



Faculty of Civil, Geo and Environmental Engineering
Chair for Computation in Engineering
Prof. Dr. rer. nat. Ernst Rank

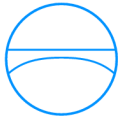
Radiation Transport in a Mosaic Crystal: Numerical Solution Based on Spectral Col- location Method

Yun Yvonna Li

Master's thesis

for the Master of Science program Computational Mechanics

Author: Yun Yvonna Li
Matriculation number: 03665138
Supervisor: Prof. Dr. rer. nat. Ernst Rank
Prof. Dr. Folkmar Bornemann
Dr. Joachim Wuttke
Date of issue: 01. May 2016
Date of submission: 31. December 2016



Involved Organisations



Chair for Computation in Engineering
Faculty of Civil, Geo and Environmental Engineering
Technische Universität München
Arcisstraße 21
D-80333 München

Declaration

With this statement I declare, that I have independently completed this Master's thesis. The thoughts taken directly or indirectly from external sources are properly marked as such. This thesis was not previously submitted to another academic institution and has also not yet been published.

München, December 31, 2016

Yun Yvonna Li

Yun Yvonna Li
Oskar von Miller Ring 25
D-80333 Munich
e-Mail: yvonna.li@tum.de

Acknowledgements

This thesis would not be possible without the support, guidance, and encouragement from many people, to whom I am deeply indebted.

The first person I would like to thank is Dr. Wuttke from the Jülich Neutron Research Center for his continual help and patience, and for his explanations concerning the theoretical foundation of neutron transport and related mathematical models.

I would also like thank Professor Bornemann for his insights on all matters related to Chebyshev polynomials and discretization.

This thesis would also not be possible without the support of Professor Rank and his approval to go ahead with this topic.

Last but not least, I would like to thank Maomao, dear friends and family in Munich and in Canada, who had to endure my constant complaining through the debugging and writing process.

Contents

1	Introduction	2
2	Physical Motivation	4
2.1	Diffraction of X-Ray	4
2.2	Bragg Reflection	5
2.3	Advent and Development of Neutron Optics	5
2.4	Mosaic Crystals	6
2.4.1	Darwin-Hamilton Equations	7
3	Mathematical Model	10
3.1	Generalized Darwin-Hamilton Equation	10
3.2	Transfer Functions	11
3.2.1	Transfer Function of a Single Crystalline Block	11
3.2.2	Transfer Function of an Infinitesimal Volume Element	12
3.3	Attenuation Coefficient and Reflection Operator	14
4	Spectral Collocation Method	15
4.1	Function Approximation	16
4.2	Spectral Method	17
4.2.1	Spectral Accuracy	17
4.2.2	Basis Functions	18
4.2.3	Minimizing the Residual Function	18
4.2.4	Strong and Weak Formulation of Differential Equation	19
4.2.5	Constructing a Spectral Method	20
4.3	Chebyshev Polynomials	20
4.3.1	Gauss Integration and Collocation Points	21
4.3.2	Derivatives	22
5	Numerical Discretization	24
5.1	Discretization of Azimuthal and Polar angles	24
5.1.1	Reflection Kernel	25
5.1.2	Discrete Attenuation Coefficient	27
5.1.3	Discrete Reflection Operator	27
5.2	Discretization in Z	28
5.3	Assemblage of Overall Matrix	29
5.3.1	Insertion of Linear Operators	30
5.4	Application of Dirichlet BC	31
5.5	Solution of System	31

6	Implementation	36
6.1	Matrix Generator	36
6.2	Reflection Kernel	37
6.3	Chebyshev Polynomial	38
6.4	Boundary Condition	38
6.5	Matrix Solver	39
7	Results	40
7.1	1D Darwin-Hamilton Equations	41
7.2	Discrete Bragg Reflectivity	42
7.3	Fully 3D results	43
	7.3.1 Effect of Bragg Reflectivity and Attenuation Coefficient	45
	7.3.2 Rocking Curves	45
8	Conclusion	56
A	Crystalline Structure	58
A.1	Bragg Planes	59
A.2	Dislocation	59
B	Analytical Solution by Sears	61

Notation

- \mathbf{k} denotes the wave vector
- $\hat{\mathbf{k}}$ denotes the (unit) direction vector
- k denotes the wave number
- θ denotes the polar angle
- φ denotes the azimuthal angle
- \mathbf{r} denotes the real space coordinates
- z denotes depth in real space
- Ψ denotes the radiation intensity field in phase-space
- $\hat{\mathbf{u}}$ denotes the mosaic block orientation as normal vectors.
- θ_B denotes the Bragg angle (material parameter)
- θ_{in} denotes the polar angle of collimated incoming beam
- φ_{in} denotes the azimuthal angle of collimated incoming beam
- P denotes the Debye-Waller factor with dimension of wavenumber
- d denotes the thickness of crystal slab
- μ denotes Bragg reflectivity
- σ denotes attenuation coefficient

Chapter 1

Introduction

Since the discovery of neutrons in first half of the 20th century, neutron scattering and neutron optics have developed into a flourishing field by its own right with many neutron research centers around the world. As a fundamental particle, there are many properties unique to the neutron that makes it useful for investigation across different scientific disciplines, for example material science, chemistry of solid state matter, fundamental physics, etc.

There are two broad categories of neutron scattering that can be applied to study different aspects of the matter under consideration. The topic under consideration in this thesis is elastic neutron scattering. Like any other beams of light, when a neutron beam interact with a sample, the neutron can undertake one of three routes: transmission through the sample, absorption by the sample, or scattering where direction of propagation is deviated.

During elastic neutron scattering, there is no energy loss of the neutron beams inside the sample under study. This type of neutron propagation is also known as neutron diffraction, and it is used to study the underlying atomic or magnetic structure of materials. The underlying principle used to model neutron diffraction is the Bragg condition, originally developed for X-Ray diffraction.

More specifically, many neutron scattering instrument feature a monochromator, which often contains mosaic crystals (crystals with dislocation imperfections). The mathematical model underlying neutron diffraction by these mosaic crystals have been written down since the last century. But due to numerical intricacies, there has not been an effort to solve the full set of Darwin-Hamilton Equations completely. Based on the latest developments made in [Wut14], this thesis aims to solve the generalized Darwin-Hamilton Equations using a variant of the spectral collocation method based on Chebyshev polynomials and discretization scheme. The numerical solution package is written as a stand-alone application using C++.

The organization of this thesis follows closely the work flow outlined in Figure 1.1. Following the introduction in this Chapter, Chapter 2 will outline the physical system and explain all relevant ideas that have contributed to our current understanding of the physics of neutron radiation inside the mosaic crystal. Then Chapter 3 will review the mathematical formalism used to model the physics, as laid down by J.Wuttke in [Wut14]. Chapter 4 will outline the basic ideas of spectral methods, with focus on the collocation method on the Chebyshev grid.

Having laid down all the theoretical foundation, Chapter 5 will establish the formalism used

for the set of discrete equations and explain in detail the discretization scheme used inside the solution package. Then Chapter 6 will describe the relevant details concerning the solution package with focus on a number of essential algorithms. Finally, numerical results are presented in Chapter 7, where validation and verification of the discrete solution are performed by comparison with analytical approximations found in literature. The thesis closes with conclusion remarks in Chapter 8.

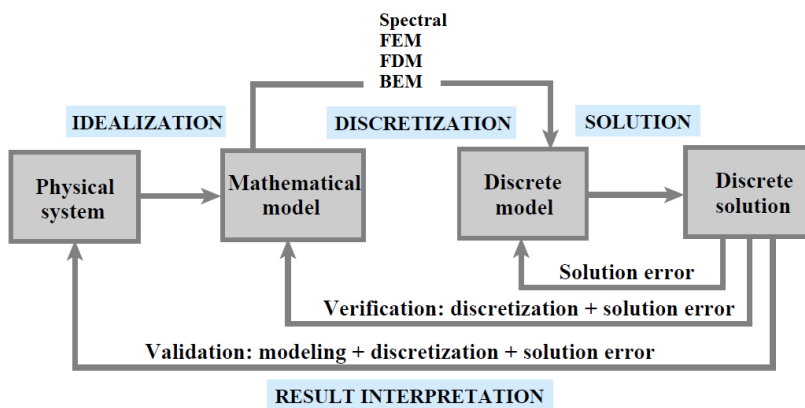


Figure 1.1: Main stages of computer-based simulation [Fel]

Chapter 2

Physical Motivation

This chapter will highlight some key discoveries made in the past leading up to the current state of neutron optics. The first of such notable discoveries is the diffraction of X-Ray by crystals. A simple interpretation of this phenomenon was made by Bragg soon after. The advent of neutron optics came a couple of decades later. Next, current applications in the field of optimization of neutron optic instruments giving reason to this thesis is outlined. Finally, this section will introduce a model for an ideally imperfect mosaic crystal.

Diffraction of X-Ray

Diffraction of light has been observed back in Newton's days, and Newton himself had expounded a corpuscular theory of light. Essentially, a 'straight' beam of light is known to 'bend' and 'spread around' a corner or through an slit with approximately the same size as the wavelength of the light shone. Indeed, all waves, including sound waves and water waves demonstrate this property. The phenomenon of diffraction was first explained qualitatively by the Huygen-Fresnel principle, which also successfully explained the laws of reflection and refraction. A sketch of a two-slit diffraction pattern, published by Thomas Young in 1803, is shown in Figure 2.1. Young's work provided further proof for the acceptance of the wave theory of light.

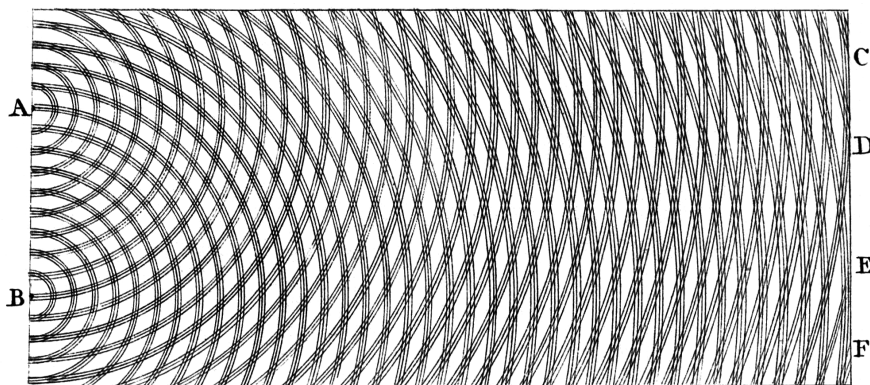


Figure 2.1: Illustration of Two Slit Diffraction Pattern [Rot03]

In 1895 Wilhelm C. Röntgen discovered the X-Ray. Scientists since then began to observe many properties that suggest X-Ray is also a form of electromagnetic wave. A decisive piece of proof that helped to confirm this hypothesis was discovered by Max von Laue, Paul Knipping and Walter Friedrich in 1912: diffraction of X-Ray by crystals.

Before Laue's discovery, scientists have already hypothesized that wavelength of X-Ray is in the range of 10^{-10} to 10^{-11} m [NM116], which is in the order of interstitial distance between molecules of a solid. While Laue won the Nobel Prize in Physics in 1914 for his discovery, it was William H. Bragg and William L. Bragg (father and son) who provided a simple and elegant way to explain this phenomenon, using the idea of lattice planes in crystals. They won the Nobel Prize in 1915 for their work, now known as the Bragg formulation of X-Ray diffraction.

Bragg Reflection

The Braggs agreed with Laue that the repetitive structure of solid crystals acted as diffractive grating. However, crystals is more complicated than the ordinary line gratings which are simply parallel lines spaced out evenly. The microscopic structure inside a crystal is 3D and the effect is diffraction by 3D grating. Laue approached the problem directly and derived a mathematical expression for the intensity field of waves incident on a set of particles arranged on a space lattice, and the expression agreed with his experimental results.[W.H15]

The Braggs successfully reduced the complexity of the problem. Their idea can be explained using Figure 2.2. Essentially, molecules within the crystal form lattice planes, and if a wave passes over the crystal, all the particles in one plane combine to reflect it. Let the distance between repeating lattice planes be d_h , then two waves reflected by two neighbouring planes are offset from each other by $2d_h \sin \theta_B$. In order for constructive inference to happen, this offset need to a multiple of wave length λ . This effect is summarized by Equation 2.1. θ_B denotes the Bragg angle, which is the angle that the incident wave makes with the Bragg plane. Important to note is that this explanation assumes that the crystal is perfectly crystalline.

$$n\lambda = 2d_h \sin \theta_B \quad (2.1)$$

For definition of the crystal lattice and calculation of distance between lattice planes d_h , please see Appendix A.

Advent and Development of Neutron Optics

In 1944, mirror reflection of thermal neutrons was observed for the first time [Sea89]. Since then, neutron radiation has been observed to demonstrate all the classical optical phenomena that light and X-ray demonstrate, including reflection, refraction, and diffraction. Because X-Ray and neutron radiation have similar wavelengths, diffractive grating by crystals can be observed for both. Therefore Bragg condition is applicable to both X-Ray and neutron wave. Bragg scattering of neutrons from a crystal of known structure can be used to produce beams

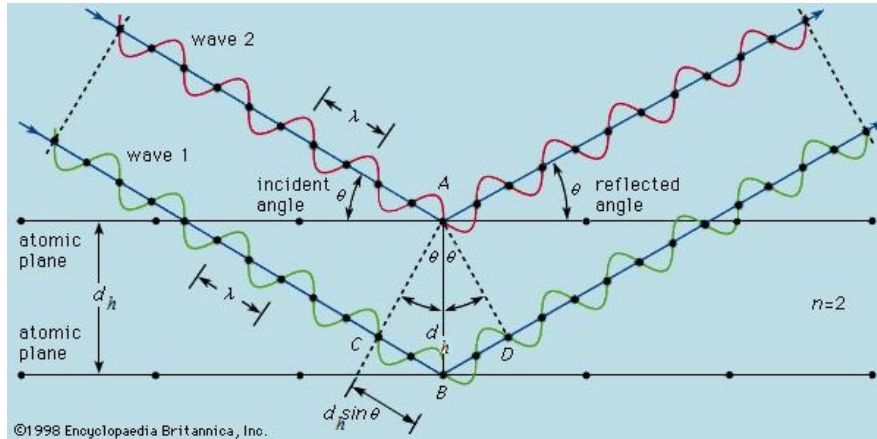


Figure 2.2: Illustration of Bragg Reflection [N.W76]

of neutrons with specified wavelength (λ). Conversely, measuring the diffraction pattern of the reflected beam from a crystal allows us to determine the crystalline structure, including the lattice constant d_h .

Up to now, knowledge of how neutrons propagate in solids have engendered the development of a field of research that manipulate neutron beams for applications in basic research through the use of neutron-optical devices. Each such device is based on one or more principle optical phenomena. Under the broad categorization of diffraction, Bragg scattering of neutrons give rise to instruments such as monochromators, polarizers and filters. The current work is geared towards the optimization of neutron optic monochromators. Monochromators are used all areas of optics: they can produce collimated, monoenergetic beams of light. [Sea89]

Mosaic Crystals

Shortly after the discovery of diffraction of X-ray by crystals, it has been observed that Bragg reflection in single crystals differed significantly from theoretical predictions.

In 1922, Charles Galton Darwin (grandson of Charles Robert Darwin) proposed that this discrepancy is due to the incorrect assumption that crystals are ideally perfect. Instead, he proposed that a single crystal is composed of a large number of ‘mosaic blocks’. Darwin introduced a mathematically tractable model of the mosaic crystal, which is subsequently known as ‘ideally imperfect’. A schematic of the theory of dislocation used to explain mosaicity can be found in Appendix A.

This model of the ideally imperfect mosaic crystal assumes that each of the mosaic blocks that make up the single crystal is thin and orientationally disordered. Consequent implication of the thin crystal block is that a kinematical diffraction model is now applicable. The kinematical diffraction model assumes multiple Bragg reflections within a crystal block to be negligible, i.e. primary distinction, reduction in the Bragg peak intensity, and other effects arising from the coherent superposition of the multiple reflection within the block are all negligible. [Sea89]

Darwin-Hamilton Equations

Another consequence of assuming the ideally imperfect model of a mosaic crystal is that neutrons inside the crystal will scatter incoherently between the mosaic blocks. More explicitly, the transport of neutrons between the blocks behave like particles until they leave the crystal. Therefore, neutron distribution can be modeled by a transport equation similar to the Boltzmann Equation which was originally developed for the Kinetic Theory of Gas. This steady state transport equation is given by Equation 2.2, which was published by Hamilton in 1957 [Ham57].

$$\hat{\mathbf{k}}_{\pm} \nabla \psi_{\pm} = \mu \psi_{\mp} - \nu \psi_{\pm} \quad (2.2)$$

Figure 2.3 shows the schematic of the geometry assumed in the original Hamilton-Darwin Equations. This is also the same geometry used in the rest of the thesis.

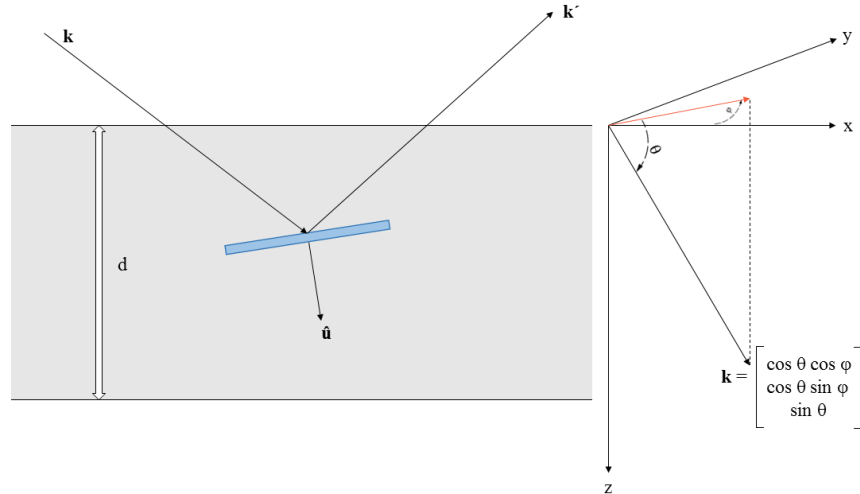


Figure 2.3: Schematic of geometry used in boundary value problem

In Equation 2.2, the fundamental quantity of interest is ψ , which represents the phase-space distribution function of the number of neutrons present in an infinitesimal volume element. I.e., ψ represents the flux field, which is equal to the intensity field in steady state. $\hat{\mathbf{k}}$ is used to denote unit direction vectors. The hat over the vector ' \mathbf{k} ' indicates that the vector has normalized magnitude. $\hat{\mathbf{u}}$ indicates the normal vector that defines the mosaic block orientation.

As part of the notation convention which will be applicable to throughout this work, $+$ is used to indicate a beam propagating in the same direction as the incident wave and $-$ indicates a beam propagating in the direction of the diffracted wave. \pm is applicable at the global scale. Another distinction is made at the local scale between $\hat{\mathbf{k}}$ and $\hat{\mathbf{k}}'$.

Figure 2.4 provides an schematic of multiple reflection within a mosaic crystal in plane. Neutrons that have been reflected an even number of times (including 0) contribute to the 'transmitted' beam. Neutrons which have been reflected an odd number of times contribute to the 'reflected' beam.

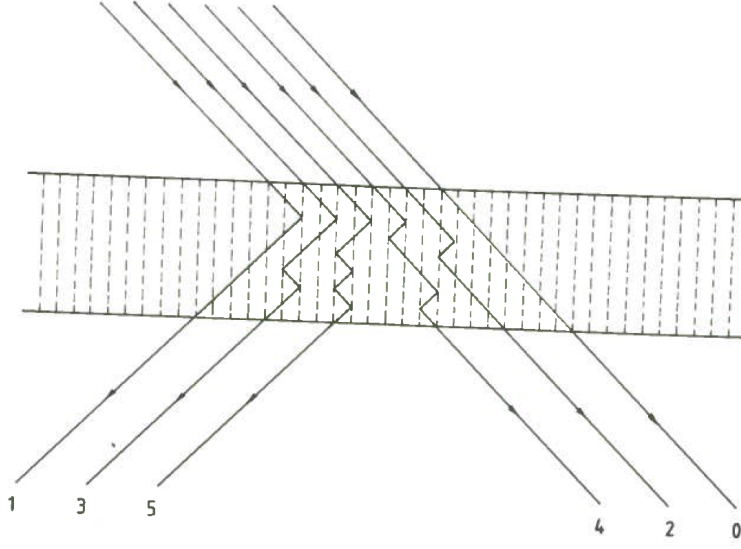


Figure 2.4: Schematic of multiple reflection inside a perfect crystal

There are also two coefficients in Equation 2.2: μ and ν . μ is the Bragg reflectivity, which accounts for gains in intensity by Bragg scattering. $\nu = \mu + \sigma_{abs} + \sigma_{inel} + \sigma_{dif}$ is the attenuation coefficient, which accounts for losses by Bragg scattering, absorption, inelastic scattering, and diffuse scattering.

Implicitly, Equation 2.2 confines $\hat{\mathbf{k}}_{\pm}$ and the block normal to a plane. Looking at Figure 2.3, convention establishes the plane to be the xz plane. z is defined to be in direction of slab thickness, d . In a fixed scattering plane, there can only be one reflected angle that satisfies the Bragg condition for a given incident angle.

To be more explicit, let us consider scenario I: we have an ideally perfect crystal in plane. In scenario I, Bragg's law states that the direction of the incident beam must be equal to the Bragg angle (a material constant) θ_B ; and there can only be one reflected beam direction.

Next, we consider scenario II: we have a mosaic crystal in plane. In scenario II, θ_B is still constant, but now the crystal consists of an assembly of crystalline blocks each with its own $\hat{\mathbf{u}}$. The assembly of mosaic blocks is modeled using a suitable statistical distribution $W(\hat{\mathbf{u}})$. The incident beam and reflected beam with directions $\hat{\mathbf{k}}$ and $\hat{\mathbf{k}}'$ is related via $\hat{\mathbf{u}}$ using the Bragg-Laue condition given in Equation 2.3.

$$\hat{\mathbf{k}}' = \hat{\mathbf{k}} - 2 \sin \theta_B \hat{\mathbf{u}}. \quad (2.3)$$

In scenario II, we are allowed to have more than one incident beam direction $\hat{\mathbf{k}}$, but for a given $\hat{\mathbf{k}}$ there is still only one allowable $\hat{\mathbf{k}}'$. Analytical solution for scenario II was published by V.F Sears in 1997 [Sea97] where the in plane problem was solved for a specific set of boundary conditions.

Scenario II is still only a crude approximation to reality. Realistically, crystals are fully 3D

objects. Let us consider scenario III: we have a mosaic crystal in 3D. In scenario III, a fixed $\hat{\mathbf{k}}$ can produce a stencil of different $\hat{\mathbf{k}}'$ which all satisfy the Bragg condition by allowing out-of-plane reflections. More explicitly, after the first reflection, the group of reflected beams form a 1D curve; after the second reflection, the twice reflected beams form a 2D surface.

Until recently, solution to the full 3D problem of multiple Bragg reflection within a thick mosaic crystal by neutron radiation has not been attempted. The current work is built largely on the developments published by J. Wuttke in 2014 [Wut14], where he derived the set of generalized Darwin-Hamilton equations which explicitly incorporates the effect of out-of-plane scattering described in scenario III.

Chapter 3

Mathematical Model

Compared to the original Darwin-Hamilton equations, the generalized Darwin-Hamilton equations incorporate wave vector ($\hat{\mathbf{k}}$) dependency of neutron intensity by considering out-of-plane reflections. In the most general case, neutron intensity $\psi := \psi(\mathbf{k}, \mathbf{r})$ is a function of spatial coordinates \mathbf{r} and wave vector \mathbf{k} . In the current formulation treated by this thesis, we consider a slab geometry where \mathbf{r} is reduced to one spatial coordinate z because we do not consider lateral displacement of the multiple reflected beams. \mathbf{k} is reduced to 2D unit vector $\hat{\mathbf{k}}$ because the transport equation only explicitly considers elastic Bragg scattering. This reduces the dimensions of our problem and $\psi := \psi(\hat{\mathbf{k}}, z)$. Furthermore, we are only interested in the steady state solution and the Bragg reflection geometry (instead of the Laue transmission geometry). Figure 2.3 is an example of Bragg reflection geometry.

This chapter will list and explain all relevant equations in detail, starting with the generalized Darwin-Hamilton Equations and Dirichlet boundary conditions. Then transfer functions and reflectivity will be exposted. Finally, expressions for attenuation coefficient and the reflection operator are derived. This chapter follows closely the formalism established in [Wut14] and [F.B].

Generalized Darwin-Hamilton Equation

The generalized Darwin-Hamilton Equations give a macroscopic description of neutron radiation within a thick mosaic crystal slab. This equation is applicable to any material medium that is homogeneous at the macroscopic scale.

$$\pm \partial_z \psi_{\pm}(\hat{\mathbf{k}}, z) = -\nu(\hat{\mathbf{k}}) \psi_{\pm}(\hat{\mathbf{k}}, z) + R(\psi_{\mp})(\hat{\mathbf{k}}, z) \quad (3.1)$$

Here ∂_z denotes partial derivative with respect to z . $\nu(\hat{\mathbf{k}})$ is the attenuation coefficient. $R(f)$ is the reflection operator on the function f . $\nu(\hat{\mathbf{k}})$ and $R(f)$ are generalized ν and μ from Equation 2.2. Expressions of $\nu(\hat{\mathbf{k}})$ and $R(f)$ will reflect the structure of the specific material.

In matrix form, the set of equation becomes

$$\begin{pmatrix} \partial_z + \nu & -R \\ -R & -\partial_z + \nu \end{pmatrix} \begin{pmatrix} \psi_+(\hat{\mathbf{k}}, z) \\ \psi_-(\hat{\mathbf{k}}, z) \end{pmatrix} = 0 \quad (3.2)$$

The physical geometry at hand translates well into a idealized model, which is an infinite slab with definite thickness.

A physically meaningful model would specify the intensity distributions at the two surfaces of the slab: $z = 0$ and $z = d$. This corresponds to two separate Dirichlet boundary conditions.

The two boundary conditions are given by

$$\psi_+(\hat{\mathbf{k}}, z = 0) = \psi_i(\hat{\mathbf{k}}) \quad (3.3)$$

$$\psi_-(\hat{\mathbf{k}}, z = d) = 0 \quad (3.4)$$

Transfer Functions

In order to arrive at a macroscopic description of the crystal slab given by the set of integro-differential equations, it is necessary to first consider a microscopic model of the mosaic crystal. At this microscopic level, we are able to obtain the transfer function of a single thin crystal block, $\mu_{\hat{\mathbf{u}}}(\mathbf{k}', \mathbf{k})$. To bridge the gap between the microscopic and macroscopic description, the transfer function of an infinitesimally thin crystal layer, $\mu(\hat{\mathbf{k}}', \hat{\mathbf{k}})$, is obtained by averaging over block orientations.

Main results which are directly used in later chapters are highlighted in this section. For detailed derivation, please refer to [Wut14].

Transfer Function of a Single Crystalline Block

At the smallest scale, we consider a single crystalline block which is so thin that kinematical approximation applies and multiple reflections within the block is negligible. For a given block orientation $\hat{\mathbf{u}}$, the transfer function $\mu_{\hat{\mathbf{u}}}(\mathbf{k}', \mathbf{k})$ defines the probability per unit length (\mathbf{r} is a function of z only in the slab geometry) that a neutron with incoming wave vector \mathbf{k} is scattered into an infinitesimal phase-space volume around \mathbf{k}' .

$$\mu_{\hat{\mathbf{u}}}(\mathbf{k}', \mathbf{k}) = \frac{P^4}{k^2} \delta(\mathbf{k}' - \mathbf{k} + 2k \sin \theta_B \hat{\mathbf{u}}) \delta(k' - k) \quad (3.5)$$

Here P is a material constant with dimension of wavenumber.

Equation 3.5 follows the work of Sears [Sea89], where only elastic scattering is considered; this is expressed by the second delta function where wave numbers of the incoming and reflected beam are forced to be equal. The first Dirac function $\delta(\mathbf{k}' - \mathbf{k} + 2k \sin \theta_B \hat{\mathbf{u}})$ ensures that \mathbf{k} , \mathbf{k}' and $\hat{\mathbf{u}}$ obeys the Laue-Bragg condition (Equation 2.3).

Transfer Function of an Infinitesimal Volume Element

Having obtained an expression for a single crystalline block, it is necessary to consider an infinitesimal volume element. In our formulation, this volume element is a thin slab with thickness of dz . Inside this element, there are many crystalline blocks with a distribution of orientation $\hat{\mathbf{u}}$. Therefore the transfer function of the infinitesimally thin slab is

$$\mu(\mathbf{k}', \mathbf{k}) = \int W(\hat{\mathbf{u}}) \mu_{\hat{\mathbf{u}}}(\mathbf{k}', \mathbf{k}) d\hat{\mathbf{u}} \quad (3.6)$$

Equation 3.6 takes the average of Equation 3.5 over $\hat{\mathbf{u}}$, where $W(\hat{\mathbf{u}}_{\mathbf{k}\beta})$ is the isotropic distribution of block orientations around $\hat{\mathbf{u}} = \hat{\mathbf{z}}$. A straightforward evaluation of Equation 3.6 would entail integration over a unit sphere.

Looking at Equation 3.5, it can be observed that the second delta function renders the integrand nonzero only for a subset of the unit sphere. The intersection between the second delta function and the unit sphere is a circle, where the delta function constitutes a plane. Therefore it is possible to reduce the surface integral to a line integral. In the end, the reflection kernel can be given by

$$\mu_{xz}(\hat{\mathbf{k}}', \hat{\mathbf{k}}) = \bar{\mu} \int W(\hat{\mathbf{u}}_{\mathbf{k}\beta}) h_{\mathbf{k}\beta} \delta(\hat{\mathbf{k}}' - \hat{\mathbf{k}} + 2 \sin \theta_B \hat{\mathbf{u}}_{\mathbf{k}\beta}) d\beta. \quad (3.7)$$

To reach this result, first let $\hat{\mathbf{k}}$ be parameterized using spherical coordinates

$$\hat{\mathbf{k}} = \begin{pmatrix} \cos \theta \cos \varphi \\ \cos \theta \sin \varphi \\ \sin \theta \end{pmatrix} \quad (3.8)$$

Next, assume that \mathbf{k} is rotated into the x-z plane such that $\varphi = 0$ and

$$\hat{\mathbf{k}}_{xz} = \begin{pmatrix} \cos \theta \\ 0 \\ \sin \theta \end{pmatrix}. \quad (3.9)$$

Let $\hat{\mathbf{u}}$ be parameterized using

$$\hat{\mathbf{u}}_{\mathbf{k}\beta} = \begin{pmatrix} \alpha \\ \beta \\ \sqrt{1 - \alpha^2 - \beta^2} \end{pmatrix} \quad (3.10)$$

Substituting 3.9 and 3.10 into the Laue-Bragg condition (Equation 2.3), and after some numerical manipulation, we get an expression for α given by

$$\alpha_{\mathbf{k}\beta} = \sin \theta_B \cos \theta_k \pm \sin \theta_k \sqrt{\cos^2 \theta_B - \beta^2} \quad (3.11)$$

where the \pm sign in Equation 3.11 indicates the two halves of the ellipse.

In Equation 3.7, prefactor $\bar{\mu}$ is given by

$$\bar{\mu} = \frac{P^4}{k^3 \sin 2\theta_B} \quad (3.12)$$

For most applications, the distribution of $\hat{\mathbf{k}}$ is taken to be

$$W(\hat{\mathbf{u}}_{\mathbf{k}\beta}) = G(\alpha)G(\beta) \quad (3.13)$$

where G represents an even, normalized, 1D distribution function, e.g. Gaussian distribution with the mean value at 0.

$h_{\mathbf{k}\beta}$ is the amplitude correction factor given by

$$h_{\mathbf{k}\beta} = \frac{\cos \theta_B}{\sqrt{\cos \theta_B - \beta^2}} \frac{|\sin \theta_B - \cos \theta_k \alpha_{\mathbf{k}\beta}(\beta)|}{\sin \theta_k} \quad (3.14)$$

Looking at Figure 3.1, we can observe the orthographic projection of the set of $\hat{\mathbf{u}}$ satisfying Equation 2.3 onto the $\alpha - \beta$ plane. Both α and β runs from -1 to 1 . Each different colored ellipse represent a different set of $\hat{\mathbf{u}}$ that satisfy Equation 2.3 for $\theta_k = \theta_B$. The left branch indicated by the solid line is given by taking the $-$ sign in Equation 3.11; the right branch indicated by the dotted line is given by taking the $+$ sign in Equation 3.11.

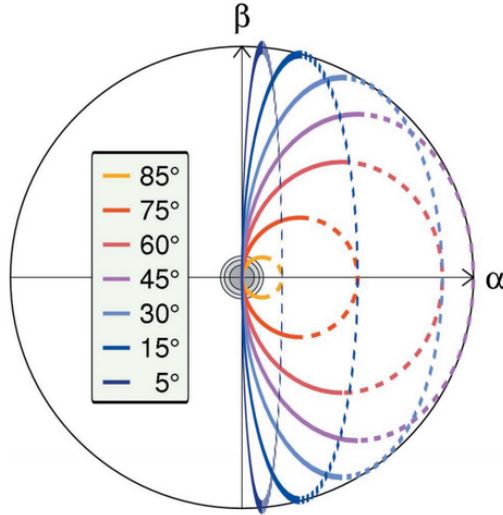


Figure 3.1: Schematic of geometry used in boundary value problem [Wut14]

The grey concentric circles represent a Gaussian distribution of block orientations, $W(\hat{\mathbf{u}})$ with standard deviation $\eta = 0.025$. The first circle encloses 90% of all $\hat{\mathbf{u}}$, the second 99%, the third 99.9%. It can be observed that the right branch of the ellipse would not generate a significant integrand in Equation 3.7, except for the limit cases of backscattering ($\theta_k \rightarrow 0$) and grazing incident ($\theta_k \rightarrow \frac{\pi}{2}$). We exclude from our considerations these two special cases and to only consider the left branch of the ellipse while integrating Equation 3.7.

Finally, for arbitrary $\hat{\mathbf{k}}$ with $\varphi_k \neq 0$ we use the following rotation matrix

$$T_k = \begin{pmatrix} \cos \varphi_k & \sin \varphi_k & 0 \\ -\sin \varphi_k & \cos \varphi_k & 0 \\ 0 & 0 & 1 \end{pmatrix} \quad (3.15)$$

where $T_k \hat{\mathbf{k}}$ gives direction vector in the x-z plane, $\hat{\mathbf{k}}_{xz}$.

The generalized reflection matrix is

$$\mu(\hat{\mathbf{k}}', \hat{\mathbf{k}}) = \mu_{xz}(T_k \hat{\mathbf{k}}', T_k \hat{\mathbf{k}}) \quad (3.16)$$

Attenuation Coefficient and Reflection Operator

Having obtained the expression of the transfer function of an infinitesimal volume element, the attenuation coefficient and the reflection kernel can be defined. As Equations 3.7 and 3.16 form the basis for majority of future calculations, $\mu(\hat{\mathbf{k}}', \hat{\mathbf{k}})$ shall be referred to as reflection kernel.

The total attenuation coefficient, $\nu(\hat{\mathbf{k}})$, contains a contribution from diffraction,

$$\mu(\hat{\mathbf{k}}) = \frac{\int \mu(\hat{\mathbf{k}}', \hat{\mathbf{k}}) d\hat{\mathbf{k}}'}{\sin \theta_k} \quad (3.17)$$

and a $\hat{\mathbf{k}}$ independent coefficient σ which accounts for all other losses. I.e.

$$\nu(\hat{\mathbf{k}}) = \mu(\hat{\mathbf{k}}) + \sigma \quad (3.18)$$

The reflection operator is defined as

$$R(f)(\hat{\mathbf{k}}) = \int \frac{\mu(\hat{\mathbf{k}}', \hat{\mathbf{k}})}{\sin \theta_{k'}} f(\hat{\mathbf{k}}) d\hat{\mathbf{k}}' \quad (3.19)$$

Chapter 4

Spectral Collocation Method

Given a physical problem, the main steps taken to solve the problem using computer based simulation has been summarized using Figure 1.1. Chapters 2 and 3 have addressed the first and second steps of this process: explain the physical problem and develop the appropriate mathematical model.

Having obtained a mathematical model, there are many reasons why this model need to be simulated by computers: one of the most common reasons is that some mathematical models of the physical system cannot be solved analytically. It is also possible the analytical solution is much more expensive to calculate than a discrete solution.

Having laid down the theoretical groundwork, our physical problem of neutron radiation in the thick mosaic crystal is now modeled by a *coupled* system of two *linear, homogeneous, first-order* integro-differential equations (Equation 3.1) along with two Dirichlet boundary conditions (Equations 3.3 and 3.4). Looking at Equations 3.1, it is reasonable to argue that a discrete solution is easier to obtain than an analytical one.

Deciding to go with discrete solution is only the beginning of a number of decisions. Spectral methods are a subset of all possible numerical methods, which include and are not limited to Finite Element Methods (FEM), Finite Difference Methods (FDM) and Boundary Element Methods (BEM). All these numerical methods are all based on the principle of using series expansions to approximate functions. An distinct difference between the different methods is the way the spatial domain is discretized. Suitable methods for problems are chosen based on the nature of the equation and physical domain under examination.

This chapter will begin with an explanation on the idea of series expansion of functions and the residual function, then go on with a brief summary of the different methods followed by some guidelines on how to construct the most appropriate spectral method. Having justified our choice of using the Spectral Collocation Method, the method will be explained in detail along with the chosen set of basis functions and discrete grid. This chapter is based loosely on various chapters from [J.P00], [C.C06], [Kop09].

Function Approximation

For a given 1D function $u(x)$, it is possible to approximate $u(x)$ using $N + 1$ number of basis functions $\phi_n(x)$ such that

$$u(x) \approx u_N(x) = \sum_{n=0}^N a_n \phi_n(x) \quad (4.1)$$

where a_n are the series coefficients. Generally, ϕ_n are orthogonal on the interval $[a, b]$ with respect to a weight function w such that

$$(\phi_n, \phi_m)_w = \int_a^b \phi_n(x) \phi_m^*(x) w(x) dx = C_n \delta_{nm} \quad (4.2)$$

where δ_{nm} is the Kronecker delta function

$$\delta_{nm} = \begin{cases} 0, & \text{if } n \neq m \\ 1, & \text{if } n = m \end{cases} \quad (4.3)$$

and $\phi_m^*(x)$ indicate the complex conjugate of $\phi_m(x)$. $(\cdot, \cdot)_w$ represents the weighted inner product of two functions, which is used repeatedly in the rest of this chapter.

More formally, expansion of u in terms of an orthogonal set of basis functions ϕ_n describes a linear transformation between u and the expansion coefficients a_n . Therefore u can be expressed both through its values in the physical space and through the coefficients in transform space.

Next, let $u(x)$ be the solution of differential or integral equation, such that

$$Lu = f(x) \quad (4.4)$$

where L represents an operator on u in the form of an integro-differential equation.

For $u(x)$ approximated by the series expansion $u_N(x)$, the error resulting from our approximation, i.e. the residual function is defined as

$$R(x; a_0, a_1, \dots, a_N) = Lu_N - f \quad (4.5)$$

R is equal to zero when $u(x)$ is the exact solution to Equation 4.4. When the exact solution is not forthcoming, the alternative is to minimize R .

Spectral Method

The classical spectral method, which works on the single tensor-product domain, have been well established since the late 70s to solve periodic differential equations (DEs) with sufficiently smooth solution. Developments made in the past decades have been aimed to accommodate discontinuous problems, and problems with complex geometries through the use of multi-domain spectral methods. The strength of classical spectral methods include superior rate of convergence, also coined as spectral accuracy.

The fast rate of convergence is due to the fact that basis functions used in classical spectral method are typically global, infinitely differentiable and nearly orthogonal. The choice of global basis functions also differentiates spectral methods from other popular methods such as the Finite Element Method (FEM) and the Finite Difference Method (FDM).

In essence, spectral collocation method is much like a very high order FDM. FDM approximates derivatives by derivating local low order polynomials interpolant at the points of interest. On the other hand, multi-domain spectral methods have been converging towards the FEM, where FEM's main strength lies in its flexibility to compute on complex geometries by breaking the spatial down to simple sub-domains.

Looking at Equation 3.1, it is clear that we have a fairly simple 1D domain with simple Dirichlet BCs. From previous investigations, it is also expected that the solution be very smooth. From this perspective, spectral methods offers itself as the perfect candidate for solving our problem numerically.

Spectral Accuracy

Without delving into proofs, spectral accuracy is presented here in contrast to algebraic convergence common for 'fixed order' methods such as FEM and FDM.

Using a fixed order method of order p to approximate a sufficiently smooth function $u \in C^k$ where C^k represents the set of all functions that is k times differentiable, we get

$$\|u - u_N\| = O(N^{-k/d}), \text{ for } k \leq p \quad (4.6)$$

Here, N is the number of DOFs, and d is the number of spatial dimensions.

For spectral methods with spectral accuracy, the restriction of $N \leq p$ is not applicable. More specifically, for $u \in C^\infty$, then

$$\|u - u_N\| = O(N^{-m}), \text{ for all } m \quad (4.7)$$

If u is analytic (e.g. power series), then convergence is even faster where

$$\|u - u_N\| = O(c^N), \text{ where } 0 \leq c \leq 1 \quad (4.8)$$

Basis Functions

One of the first components in constructing a spectral method is the set of basis functions ϕ_n . Most sets of basis functions are required to satisfy a few requirements such as orthogonality, completeness and for practical reasons, ease of calculation. Common basis functions such as the Fourier series, Chebyshev polynomials, Legendre Polynomials, etc all satisfy these basic requirements.

Beyond the basic requirements, each set of basis functions offers unique properties that make them more or less suitable for different areas of application. For periodic functions, the first preference is generally Fourier series. For non-periodic functions, Chebyshev and Legendre polynomials are often the basis of choice. All three of sets of basis functions demonstrate the so called spectral accuracy property for approximating adequately smooth functions.

Minimizing the Residual Function

The second component in constructing a spectral method is the way that the residual function is minimized. Various popular methods can be categorized under the broad label of the method of weighted residuals [C.C06], also referred to as the mean weighted residual methods [J.P00].

For a given non-negative weight function $w(x)$ and any two functions $u(x)$ and $v(x)$, the weighted inner product $(u, v)_w$ defines the most general form of the weighted residual. For u being approximated by $\phi_n(x)$ as shown in Equation 4.1, common methods vary from each other by using different choices of $w(x)$, which is also called the trial function in literature. The two most common methods include the collocation method, Galerkin, and/or Tau method depending on different ways of categorization. Under the context of residual methods, w is also referred to as test functions.

The collocation method takes the trial functions w_i to be

$$w_i(x) = \delta(x - x_i) \quad (4.9)$$

where x_i are taken to be set of interpolation or collocation points. Practically, the collocation method imposes that

$$R(x_i; a_0, a_1, \dots, a_N) = 0, \quad i = 1, \dots, N \quad (4.10)$$

As mentioned in Section 4.2, the spectral collocation method is similar to FDM where both methods can be thought to ‘interpolate’ the solution at points, which are often referred to in literature as ‘nodes’. This type of interpolating methods is also called ‘nodal’.

An alternative is to take

$$w_i(x) = \phi_i(x) \quad (4.11)$$

[J.P00] refers all methods that uses the same set of functions for both the basis and the test functions as the Galerkin. [C.C06] differentiates between the Galerkin and the Tau method

depending on whether test functions are chosen to satisfy boundary conditions individually. More explicitly, R can also be expanded by basis functions like any other function such that

$$R(x; a_0, a_1, \dots, a_N) = \sum_{i=0}^{\infty} r_i(a_0, a_1, \dots, a_N) \phi_i(x) \quad (4.12)$$

with

$$r_i = (R, \phi_i) \quad (4.13)$$

Galerkin methods minimize $R(x)$ by making first $(N+1)$ terms in Equation 4.12 equal to 0. I.e.,

$$r_i = 0, i = 0, 1, 2, \dots, N \quad (4.14)$$

The Galerkin ‘spreads the error’ over the entire domain, and is part of ‘modal’ analysis. Both Fourier and Chebyshev series of smooth functions decrease exponentially with respect to i , i.e., r_i will be very small for large N .

Strong and Weak Formulation of Differential Equation

One important consideration in choosing between different residual methods is the formulation of the differential equation (DE) under consideration. Because the collocation method satisfies the DE pointwise by enforcing $R = 0$ at x_i , the strong formulation of DE is used. In contrast, Galerkin methods requires the weak formulation of DE. Consider the following DE in strong form

$$u \frac{\partial u}{\partial x} - \nu \frac{\partial^2 u}{\partial x^2} = 0 \quad (4.15)$$

inside interval $x = [a, b]$. Equation 4.15 is in the strong form. The weak form is obtained by taking the integral of the DE against all test functions w in the test space X . I.e.,

$$\int_a^b u \frac{\partial u}{\partial x} w dx - \int_a^b \nu \frac{\partial^2 u}{\partial x^2} w dx = 0, \forall w \in X \quad (4.16)$$

To take this a step further, integration by parts on Equation 4.16 gives

$$-\frac{1}{2} \int_a^b u^2 \frac{\partial w}{\partial x} dx + \nu \int_a^b \frac{\partial u}{\partial x} \frac{\partial w}{\partial x} dx + \left(\frac{1}{2} u^2 w - \nu \frac{\partial u}{\partial x} w \right) \Big|_{x=b} - \left(\frac{1}{2} u^2 w - \nu \frac{\partial u}{\partial x} w \right) \Big|_{x=a} = 0, \forall w \in W. \quad (4.17)$$

All three formulation (Equations 4.15, 4.16, 4.17) are equivalent if the solution is sufficiently smooth. However, one of the many advantages of using the weak formulation is that the weak formulations can accommodate less smooth solutions. Another reason is for choosing

Equation 4.17 is that lower order derivatives are required after integration by parts is applied, significantly reducing the complexity of implementation.

Constructing a Spectral Method

Between the different basis functions and methods of weighted residual, it is possible to combine the two components to make a list of permutations: Fourier Galerkin, Chebyshev Collocation, etc. Constructing an appropriate method is matter of choosing what is most suitable for the particular equation at hand. In general, it is also good practice to get to know the solution to the problem as much as possible before applying numerical techniques. Knowing how the solution should look like is indispensable in trying to approximate it.

Relying on rules of thumb found in literature: smooth solution and first order derivative excludes the need for Galerkin methods where the weak formulation of the DE offers no advantage. Simple Dirichlet BCs can also be quite easily implemented using the collocation method. Chebyshev polynomials are chosen in this work mainly out convenience, where there are an abundance of literature with simple and fast algorithm for computing the differentiation matrix.

Chebyshev Polynomials

Chebyshev polynomials can be understood as Fourier transforms in disguise. Fourier basis functions are complex exponentials e^{inx} and expansion take the form

$$S_N(x) = \sum_{n=-N/2}^{N/2} \hat{s}_n e^{inx} = \sum_{n=-N/2}^{N/2} \hat{s}_n (\cos nx + i \sin nx) \quad (4.18)$$

Chebyshev Polynomials are in fact Cosine series with a change of variable, i.e.,

$$T_k(x) = \cos(k \cos^{-1}(x)) \quad (4.19)$$

Using a recurrence formula, the Chebyshev polynomials can also be generated using

$$T_{k+1}(x) = 2xT_k(x) - T_{k-1}(x) \quad (4.20)$$

where the first and second terms are $T_0 = 1$ and $T_1 = x$.

Independent from Fourier transforms, the Chebyshev polynomials can be derived as a subclass of Jacobi polynomials, which are polynomial eigenfunctions to the so called singular Sturm-Liouville problem on the interval $(-1, 1)$. The Sturm-Liouville theorem guarantees that these eigenfunctions form an orthogonal basis for square integrable functions, specifically $L_w^2(a, b)$, which is exactly what we need as a set of useful basis functions for function approximation.

Furthermore, the Sturm-Liouville theorem states that “eigenfunctions of singular SL operator allow spectral accuracy in expansion of any smooth function”, and when the eigenfunctions

are polynomials, they form “natural extension of the Fourier system for approximation of nonperiodic functions” [C.C06].

Gauss Integration and Collocation Points

In the classical formulation of Gauss integration, we let $x_0 < x_1 < \dots < x_N$ be the roots of $(N + 1)$ th orthogonal polynomial p_{N+1} , and let w_0, \dots, w_N be the solution to the linear system, such that

$$\sum_{j=0}^N (x_j)^k w_j = \int_{-1}^1 x^k w(x) dx, \quad 0 \leq k \leq N \quad (4.21)$$

Then for $w_j > 0$ for $j = 0, \dots, N$

$$\sum_{j=0}^N p(x_j) w_j = \int_{-1}^1 p(x) w(x) dx, \quad \text{for all } p \in P_{2N+1} \quad (4.22)$$

In the classical version, x_j are inside the interval $(-1, 1)$. Two variations on the Gauss integration forces $x_0 = -1$ and/or $x_N = 1$: Gauss- Radua and Gauss- Lobatto.

When orthogonal polynomials are taken to be Chebyshev polynomials, Gauss integration gives

$$x_j = \cos\left(\pi \frac{2j+1}{2N+1}\right), \quad j = 0, 1, \dots, N \quad (4.23)$$

and

$$w_j = \frac{\pi}{N+1} \quad (4.24)$$

Gauss- Lobatto integration which makes $x_0 = -1$ and $x_N = 1$ gives

$$x_j = \cos \frac{j\pi}{N}, \quad j = 0, 1, \dots, N \quad (4.25)$$

and

$$w_j = \begin{cases} \frac{\pi}{2N}, & j = 0, N \\ \frac{\pi}{N}, & j = 1, \dots, N-1 \end{cases} \quad (4.26)$$

For boundary conditions imposed strongly at $x_0 = -1$ and $x_N = 1$, the Gauss-Lobatto points are used. Imposing the location of two abscissas reduced the number of degrees of freedoms, therefore G-L integration has lower precision than classical Gauss integration. G-L integration is exact for polynomials of degree $2N - 1$ or less and Gaussian integration is exact

for polynomials of degree or less $2N + 1$. Equation 4.25 gives the so called Chebyshev points, also known as Chebyshev-Lobatto points.

The usefulness of Equation 4.25 lies in the fact that these roots/abscissa/nodes of Gauss-type integrations gives the optimal collocation points for satisfying Equation 4.10. More explicitly, in the collocation method, a smooth function u on $[-1, 1]$ is represented by values of $u(x_j)$ at x_j taken to be Gauss-type integration points.

For any u, v continuous on $[-1, 1]$, let

$$(u, v)_N = \sum_{j=0}^N u(x_j)v(x_j)w_j \quad (4.27)$$

Then Gauss-type integration implies that

$$(u, v)_N = (u, v)_w, \text{ if } u, v \in P_{2N+\delta} \quad (4.28)$$

where $\delta = 1$ for Gauss integration and -1 for Gauss-Lobatto.

Derivatives

Let an interpolating polynomial approximating u be $I_N u$. $I_N u \in P_N$ and

$$I_N u(x_j) = u(x_j), 0 \leq j \leq N \quad (4.29)$$

Then the derivative of u can be approximated by taking the derivative of the interpolating polynomial $I_N u$ such that

$$u'(x) = (I_N u)' = D_N u \quad (4.30)$$

where D_N indicates the differentiation matrix on the vector of discrete $u(x_j)$ values at the collocation points. $(I_N u)'$ is asymptotically worse approximation of u' than $I_{N-1}(u')$ for functions with finite regularity for Chebyshev (and Legendre) interpolation.

$$(D_N u)(x_i) = \sum_{j=0}^N (D_N)_{ij} u(x_j), i = 0, \dots, N \quad (4.31)$$

To calculate the differentiation matrix, D_N , we rewrite the interpolation on the Chebyshev grid using Lagrange interpolating polynomials l_j which are 1 at x_j and 0 at other interpolation points. I.e.,

$$L_N(x) = \sum_{j=0}^N u(x_j)l_j(x) \quad (4.32)$$

and

$$(L_N(x))' = \sum_{j=0}^N u(x_j) l_j'(x) = \sum_{j=0}^N D_N u(x_j) \quad (4.33)$$

Therefore,

$$D_{ij} = l_j'(x_i)$$

The first derivative on the Chebyshev-Lobatto grid at the nodes is given by Figure 4.1

$$D_N = \begin{array}{|c|c|c|} \hline \frac{2N^2+1}{6} & & \frac{1}{2}(-1)^N \\ \hline & \frac{2(-1)^j}{1-x_j} & \\ \hline & & \frac{(-1)^{i+j}}{x_i-x_j} \\ \hline -\frac{1}{2} \frac{(-1)^i}{1-x_i} & \frac{-x_j}{2(1-x_j^2)} & \frac{1}{2} \frac{(-1)^{N+i}}{1+x_i} \\ \hline & \frac{(-1)^{i+j}}{x_i-x_j} & \\ \hline -\frac{1}{2}(-1)^N & -2 \frac{(-1)^{N+j}}{1+x_j} & -\frac{2N^2+1}{6} \\ \hline \end{array}$$

Figure 4.1: Schematic of the First Chebyshev Differentiation Matrix [Tre01]

Alternatively, to minimize round off errors, the following formula can be used. In both cases, i, j are used to indicated the row and column index respectively.

$$D_N = \begin{cases} \frac{-c_i}{2c_j} \frac{(-1)^{i+j}}{\sin[(i+j)\pi/2N] \sin[(i-j)\pi/2N]}, & j \neq l \\ \frac{-x_i}{2 \sin[i\pi/N^2]}, & 1 \leq j = l \leq N-1 \\ \frac{2N^2+1}{6}, & j = k = 0 \\ \frac{-2N^2+1}{6}, & j = k = N \end{cases} \quad (4.34)$$

where

$$c_j = \begin{cases} 2, & j = 0, N \\ 1, & \text{else} \end{cases} \quad (4.35)$$

Chapter 5

Numerical Discretization

There are three main components in the generalized Darwin Hamilton Equations that need to be generated numerically: the reflection operator, the attenuation coefficient, and the differentiation matrix.

This section will start with a discussion on discretization of θ and φ , followed by numerical treatment of the reflection operator and attenuation coefficient. Then discretization in z and the differentiation matrix is discussed in detail. This section will conclude with assembly of the overall matrix, application of Dirichlet BCs, and a brief discussion on solution of the system of linear equations.

An noteworthy decision is that the same discretization scheme is used for both ψ_+ and ψ_- . This effectively halves the number of operations necessary to calculate the overall matrix compared to the case where two different discretization schemes are used. There is also no apparent advantage to be gained by using a more refined grid for either ψ_+ or ψ_- .

Discretization of Azimuthal and Polar angles

From Equation 3.8, it is apparent that the coordinate system used to describe the direction vector $\hat{\mathbf{k}}$ is akin to the common spherical coordinate system. The polar angle θ measures the angle from the xy plane to the vector. The azimuthal angle φ measures the angle from the x axis to the projection of the vector onto the xy plane. The wave number k only appears as a constant parameter.

For our domain of an infinite slab, the largest possible range of the incident beam is $\theta_+ = (0, \pi/2)$ and $\varphi_+ = [0, 2\pi)$, where $\theta_+ = 0$, the so-called grazing incident and $\theta_+ = \pi/2$, the so-called back scattering, are excluded from our theory. The Laue-Bragg condition (Eq. 2.3) gives us the range the diffracted beam to be $k_z^- = \sin(\theta_-) = \sin \theta_+ - 2k \sin \theta_B \sqrt{1 - \alpha^2 - \beta^2}$. Excluding grazing incidence, $|\sin \theta_+ - \sin \theta_B| \ll \sin \theta_B$; furthermore, distribution of $\hat{\mathbf{u}}$ limits $\alpha \ll 1$ and $\beta \ll 1$. Therefore, $k_z^- < 0$, and $\theta_- = (\pi, 3\pi/2)$. Again, $\varphi_- = [0, 2\pi)$.

Compared to the original theoretical treatment of crystal kinematics [Wut14], the equations found in Chapter 3 of this thesis are indeed only applicable to odd-order reflections, and a second set of equation is used for the even-order reflections. As seen in Figure 2.4, the main

difference in odd and even-order reflection is that diffracted beam in odd-order reflection has $k_z < 0$. The opposite holds true for the even order reflections.

By solving the two differential equations directly, we forego separate considerations for the different order reflections all together. By considering only the Bragg geometry, we are able to consider only the reflections where $k_z^- < 0$, and to clearly distinguish between the incident and diffracted beams.

In order to use the same discretization scheme for both the incident and diffracted beam, we intentionally invert the sign of k_z^- and make the range of $\theta_- = (0, \pi/2)$, the same as θ_+ . Mathematically, the two component intensity field is given below

$$\Psi(\hat{\mathbf{k}}, z) = \begin{pmatrix} \psi_+(\hat{\mathbf{k}}, z) \\ \psi_-(P\hat{\mathbf{k}}, z) \end{pmatrix} := \begin{pmatrix} \psi(\hat{\mathbf{k}}, z) \\ \psi(P\hat{\mathbf{k}}, z) \end{pmatrix} \quad (5.1)$$

where now Ψ is only defined if $k_z > 0$. P is the projection operator $1 - 2\hat{\mathbf{z}} \otimes 2\hat{\mathbf{z}}$.

The physical intensity can be recovered using

$$\psi(\hat{\mathbf{k}}, z) = \psi_+(\hat{\mathbf{k}}, z) + \psi_-(P\hat{\mathbf{k}}, z) \quad (5.2)$$

As a first attempt at solving the boundary-value problem directly, a straight-forward rectangular discretization of θ and φ is used. The solution vector is solved at the center of equi-distant intervals for both angles (θ and φ).

Reflection Kernel

The reflection kernel given by Equations 3.7 and 3.16 form the basis for calculating the reflection operator R and attenuation coefficient ν . Looking at Equation 3.7, we can see that $\mu(\hat{\mathbf{k}}', \hat{\mathbf{k}})$ is a 4th order tensor, mapping $\hat{\mathbf{k}}(\theta, \varphi)$ to $\hat{\mathbf{k}}'(\theta', \varphi')$.

This operator is also an integral in β with a Dirac function in the integrand. This greatly simplifies calculation: for a given $\hat{\mathbf{k}}^*(\theta, \varphi)$, there is a single β^* value where the integrand is non-zero. In other words, there is one to one mapping between β and $\hat{\mathbf{k}}'(\theta', \varphi')$ for a given $\hat{\mathbf{k}}^*$.

Mathematically,

$$\mu_{xz}(\hat{\mathbf{k}}', \hat{\mathbf{k}}^*) = \bar{\mu} \int W(\hat{\mathbf{u}}_{\mathbf{k}^*\beta^*}) h_{\mathbf{k}^*}(\beta^*) \delta(\hat{\mathbf{k}}' - \hat{\mathbf{k}}^* + 2 \sin \theta_B \hat{\mathbf{u}}_{\mathbf{k}^*\beta^*}) d\beta = \bar{\mu} W(\hat{\mathbf{u}}_{\mathbf{k}^*\beta^*}) h_{\mathbf{k}^*}(\beta^*) \quad (5.3)$$

for

$$\hat{\mathbf{k}}' = \hat{\mathbf{k}}^* - 2 \sin \theta_B \hat{\mathbf{u}}_{\mathbf{k}^*\beta^*}. \quad (5.4)$$

Practically, for each given $\hat{\mathbf{k}}^*$, we are able to calculate and store the reflection kernel as a list of triplets: (w, θ', φ') where w is the value of the integrand at single β^* value where the integrand is non-zero.

Since we are interested in discrete solution of the problem, we perform this β integration at discrete β_u with $\Delta\beta$ (at least one) orders of magnitude smaller than $\Delta\theta$ and $\Delta\varphi$. Again, we use an equidistant grid for β_u . Since we know that the integrand of reflection kernel contains $W(\hat{\mathbf{u}}_{\mathbf{k}\beta}) (= G(\alpha)G(\beta))$, an isotropic distribution of block orientations, we are able to reduce the indefinite integral to a definite integral with bound on β determined by a practical statistical value (± 3 standard deviation) where outside this bound, integrand is known to be decrease rapidly to zero.

At this point, we are able to generate N_β number of triplets for each given $\hat{\mathbf{k}}^*$ and each entry contains a coefficient w with a pair of corresponding real-valued $\hat{\mathbf{k}}'(\theta', \varphi')$. Since we are interested in the discrete solution of ψ_\pm , we only need to compute the kernel for discrete values of $\hat{\mathbf{k}}(\theta_i, \varphi_j)$. Let this list of w indexed by β_u be named $K_{i,j}(\beta_u)$

$$K_{i,j}(\beta_u) = \bar{\mu}G(\beta_u)G(\alpha(\beta_u))h_{\mathbf{k}}(\beta_u)\Delta\beta \quad (5.5)$$

Furthermore, we also need to convert each $K_{i,j}(\beta_u)$ (a list of triplets) into a 2D matrix where each entry of the 2D matrix corresponds to a discrete $\hat{\mathbf{k}}'(\theta'_l, \varphi'_m)$. The idea is illustrated by Figure 5.1.

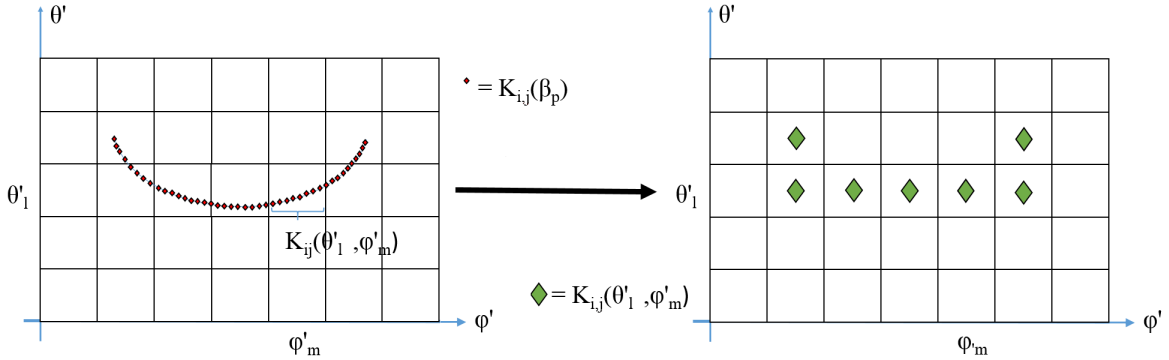


Figure 5.1: Schematic of converting $K_{i,j}(\beta_u)$ to $K_{i,j}(\theta'_l, \varphi'_m)$

Each square represents a rectangular domain $(\theta')_l = [\theta'_l, \theta'_{l+1}]$, $(\phi')_m = [\phi'_m, \phi'_{m+1}]$ and can contain more than one $K_{i,j}(\beta_u)$. The coefficient w associated with each square is simply the sum of coefficients from the different $K_{i,j}(\beta_u)$ inside the square. Let this new matrix indexed by $\hat{\mathbf{k}}'(\theta'_l, \varphi'_m)$ be named $K_{i,j}(\theta'_l, \varphi'_m)$.

Mathematically, this can be formulated using Knuth-Iverson brackets

$$K_{i,j}(\theta'_l, \varphi'_m) = \sum_{p=1}^{N_\beta} K_{i,j}(\beta_u) \llbracket \theta' \in (\theta')_l \rrbracket \llbracket \phi' \in (\phi')_m \rrbracket \quad (5.6)$$

$\llbracket \rrbracket$ representing the Knuth-Iverson brackets are given by

$$\llbracket Q \rrbracket = \begin{cases} 1, & \text{if } Q \text{ is true} \\ 0, & \text{if } Q \text{ is false} \end{cases} \quad (5.7)$$

Discrete Attenuation Coefficient

Having obtain the reflection kernel, the lineic Bragg reflectivity can be calculated by the following equation

$$\mu(\hat{\mathbf{k}}) \simeq \frac{1}{\sin \theta_k} \int \bar{\mu} G(\beta) G(\alpha) h_{\mathbf{k}}(\beta) d\beta \quad (5.8)$$

This result is obtained by exchanging the order of integration. Looking at Equations 3.6 and 3.18, it is clear that by integrating first \hat{k}' , we are able to get rid of the Dirac function and get to Equation 5.8

To calculate Equation 5.8, numerical integration in β is performed with the same equidistant β_u grid used in Section 5.1.1. Comparing Equation 5.8 with 5.5, we can see that for each discrete $\hat{\mathbf{k}}^*(\theta_i, \varphi_j)$, the integrand inside Equation 5.8 is stored discretely as $K_{i,j}(\beta_u)$. I.e., given discrete $\hat{\mathbf{k}}^*$, 5.8 can be obtained by summing over $K_{i,j}(\beta_u)$. At the end, we obtain one μ value for each discrete $\hat{\mathbf{k}}^*$. Let this discrete μ be named $M_{i,j}$, and be expressed by the following equation.

$$M_{i,j} = \frac{1}{\sin \theta_i} \sum_{p=1}^{N_\beta} K_{i,j}(\beta_u) \quad (5.9)$$

Discrete Reflection Operator

Looking at Equation 3.19, the reflection operator is understood to involve integration over $\hat{\mathbf{k}}'(\theta', \varphi')$. Since $\hat{\mathbf{k}}'$ is parameterized in the same manner as $\hat{\mathbf{k}}$ by Equation 3.8, we can perform this double integration by taking into consideration the Jacobian of our coordinate system, $\cos \theta'$. I.e.,

$$\int f d\hat{\mathbf{k}}' = \int \int f \cdot \cos(\theta') d\theta' d\varphi' \quad (5.10)$$

The discrete version is

$$\int f d\hat{\mathbf{k}}' \simeq \sum_{l=1}^{N_\theta} \sum_{m=1}^{N_\varphi} f \cdot \cos(\theta'_l) \Delta\theta' \Delta\varphi' \quad (5.11)$$

Putting Equation 3.19 and 5.11 together, the discrete reflection operator is given by

$$R_{i,j}(f) \simeq \sum_{l=1}^{N_\theta} \sum_{m=1}^{N_\varphi} \frac{1}{\sin \theta'_l} K_{i,j}(\theta'_l, \varphi'_m) \cdot f \cdot \cos \theta'_l \Delta\theta' \Delta\varphi' \quad (5.12)$$

Looking at the generalized Darwin Hamilton Equations (3.2), the reflection operator is performed on ψ_{\mp} , when ψ_{\pm} is the incoming beam and ψ_{\mp} is the outgoing beam. The discrete reflection operator makes use of the discrete reflection kernel $K_{i,j}(\theta'_l, \varphi'_m)$, indexed by $\hat{\mathbf{k}}'(\theta'_l, \varphi'_m)$. Therefore, for a given discrete $\hat{\mathbf{k}}(\theta_l, \varphi_m)$ we get

$$R_{i,j}(\psi_{\mp})(\hat{\mathbf{k}}, z) \simeq \sum_{l=1}^{N_{\theta}} \sum_{m=1}^{N_{\varphi}} \frac{1}{\sin \theta'_l} K_{i,j}(\theta'_l, \varphi'_m) \cdot \psi_{\mp}(\theta_l, \varphi_m) \cdot \cos(\theta'_l) \Delta \theta' \Delta \varphi' \quad (5.13)$$

Discretization in Z

Discretization in z follows the prescribed collocation scheme given by Chebyshev polynomials under Gauss-Lobatto integration (Equation 4.25). A noteworthy detail is that the collocation scheme and the differentiation matrix given by Figure 4.1 and by Equation 4.34 are directly applicable for $x \in [-1, 1]$. Figure 5.2 visualizes how the discretization looks like on the interval $[-1, 1]$

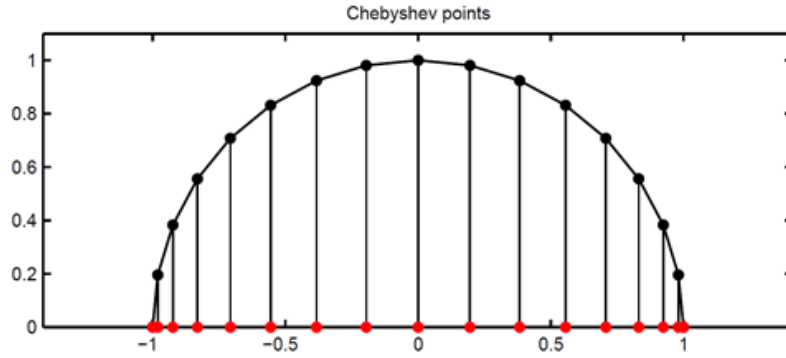


Figure 5.2: Chebyshev points on $[-1, 1]$ [Tre01]

In a realistic physical system, thickness d is a parameter with great influence on the solution. [Wut14] posits that effects of multiple reflection between the mosaic blocks would be most significant for intermediate values of d . Therefore the physical domain would be best modeled by $z \in [a, b]$ with $a < b$ and $d = b - a$. Then x can be mapped to z via

$$z = \frac{b-a}{1-(-1)}x + \frac{b+a}{1-(-1)} \quad (5.14)$$

Therefore

$$\partial z = \frac{dz}{dx} \partial x = \frac{b-a}{2} \partial x = \frac{d}{2} \partial x \quad (5.15)$$

Practically, this means that when apply Figure 4.1 or Equation 4.34, a constant factor of $d/2$ need to be applied. Finally, let the differentiation matrix be indexed using p and q , then $D_{p,q}$ is given by

$$D_{p,q} = \frac{d}{2} \cdot \begin{cases} \frac{-c_p}{2c_q} \frac{(-1)^{p+q}}{\sin[(p+q)\pi/2N_z] \sin[(p-q)\pi/2N_z]}, & p \neq q \\ \frac{-x_p}{2 \sin[p\pi/N_z]^2}, & 1 \leq p = q \leq N-1 \\ \frac{2N_z^2+1}{6}, & p = q = 0 \\ \frac{-2N_z^2+1}{6}, & p = q = N \end{cases} \quad (5.16)$$

where again N_z represents the number of discrete intervals inside $[a, b]$ and

$$c_p = \begin{cases} 2, & p = 0, N \\ 1, & \text{else} \end{cases} \quad (5.17)$$

Assemblage of Overall Matrix

Thus far, we have established the formalism for calculating the discrete attenuation coefficient $M_{i,j}$, the reflection operator $R_{i,j}$, and the differentiation matrix $D_{p,q}$. To combine these three linear operators into the overall matrix A , it is helpful to clarify the four quadrants of our overall matrix, A . Figure 5.3 helps to illustrate this idea.

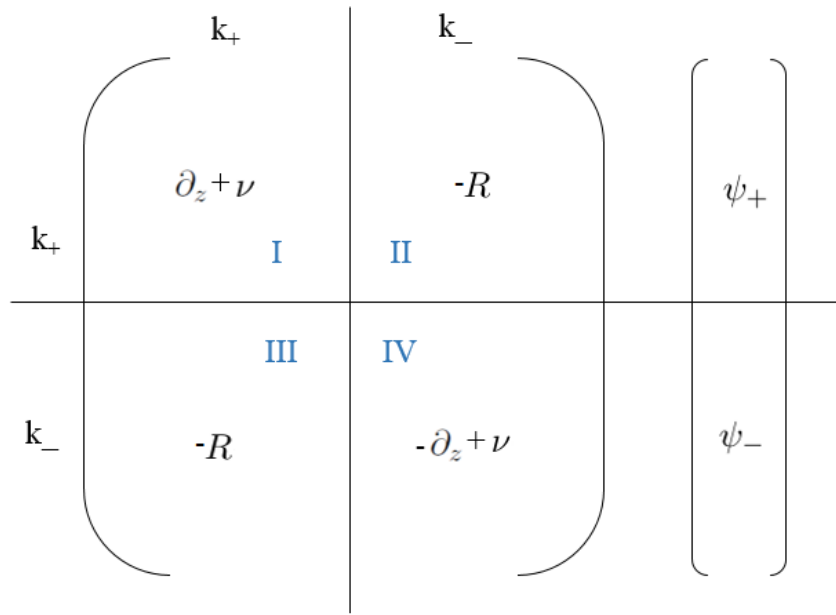


Figure 5.3: Schematic of A and x

Before the entire system of differential equation can be discretized, it is also necessary to clarify the ordering of the degrees of freedom (DOFs) in the solution vector, x .

While the ordering of DOFs is more or less arbitrary, it can have an impact on the performance of the simulation package. For this paper, the order of the DOFs is as follows: z , θ , φ . More explicitly, the solution vector looks similar to the schematic provided in Figure 5.4, where z discretization forms the outermost loop, following by θ , then φ . Normally, the solution vector is a column vector; the schematic shows a row vector to save space.

In the following subsection, the insertion of $M_{i,j}$, $R_{i,j}$, and $D_{p,q}$ are explained in detail.

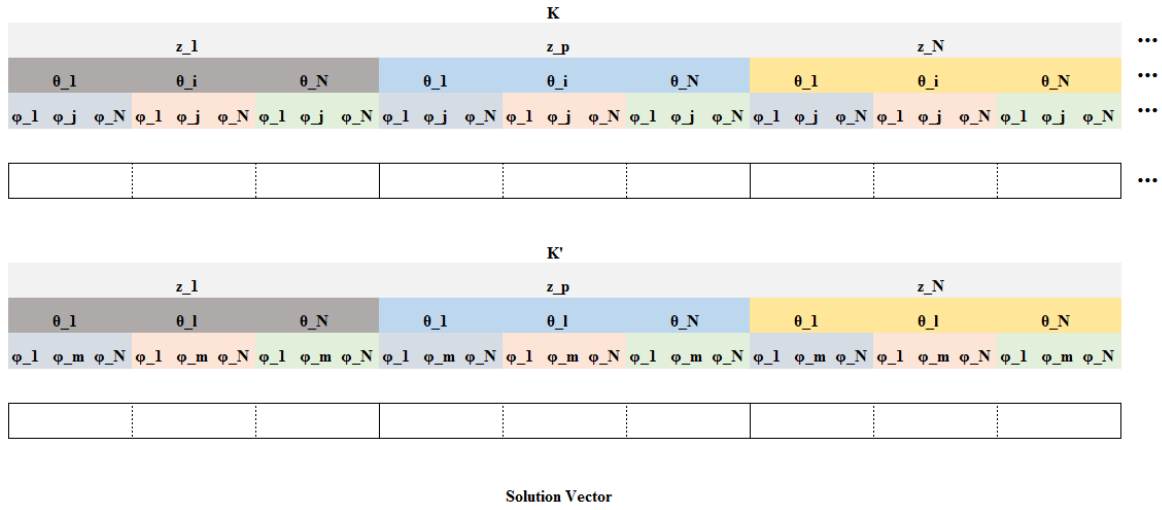


Figure 5.4: Schematic of solution vector x

Insertion of Linear Operators

The operation of $M_{i,j}$ on ψ_+ and ψ_- is a scalar multiplication on the solution vector. Therefore we expect the discrete operator in matrix form to be diagonal. As the operator is z -independent, the diagonal elements repeats itself for every z . Figure 5.5 shows the schematic for discrete $M_{i,j}$, which is placed in submatrix I and III. Each entry of $M_{i,j}$ is represented by one square. Squares with same color dictates entries with the same value of $M_{i,j}$

The operation of $R_{i,j}$ on ψ_+ and ψ_- is an integration with ψ_{\pm} inside the integrand. From Equation 5.13, it can be deduced that the coefficient of the matrix of this linear operator is given by

$$R_{i,j,l,m} = \frac{1}{\sin \theta'_l} K_{i,j}(\theta'_l, \varphi'_m) \cos(\theta'_l) \Delta \theta' \Delta \varphi' \tag{5.18}$$

Placement of $R_{i,j,l,m}$ inside the II quadrant of A is drawn in light blue in Figure 5.6. The reflection operator is decoupled in z , therefore the repeated blocks are placed in the z diagonals. The schematic hides the fact that each R block is sparse.

The operation of $D_{p,q}$ on ψ_{\pm} is decoupled in terms of θ and φ and independent of θ and φ . Therefore, the shape of the matrix is diagonal across each $\theta - \varphi$ block. Figure 5.7 helps to illustrate the placement of $D_{p,q}$ inside submatrix I and III.

As all three operators are linear, it is possible and very efficient to generate each separately, then place into the respective entry in A . Each entry in A is simply a sum over the coefficients from each of the three operators.

Application of Dirichlet BC

Our approach to enforce non-homogeneous Dirichlet boundary conditions (Equations 3.3 and 3.4) is fairly straight forward. It is done globally, taking advantage of the fact that the two integro- differential equations are linear. More formally, the idea can be expressed by Equations 5.19, where b is taken to represent the right hand side vector. The subscripts x_{homo} and x_{BC} refer to the homogeneous part of x and the part of x which comes from the Dirichlet boundary conditions.

$$\begin{aligned}
 x &= x_{homo} + x_{BC} \\
 A \cdot x &= A \cdot (x_{homo} + x_{BC}) = b \\
 A \cdot x_{homo} &= b - A \cdot x_{BC} \\
 A \cdot x_{homo} &= b_{updated}
 \end{aligned} \tag{5.19}$$

Using Equation 5.19, we are able to calculate $b_{updated}$. Then the system can be solved by deleting the corresponding rows and columns from A , x and b . This gives the reduced system: A_{red} , x_{red} , and b_{red}

Implementation of the specific set of BC shown in Equation 5.19 is illustrated in Figure 5.8. The two BCs from Equations 3.3 and 3.4 are both applied for specific z and covering all values of θ and φ . The first boundary condition corresponds to the yellow area, and the second BC to the green. The reduced system of equations is obtained by retaining only the unshaded areas in A and $b_{updated}$

Consideration of other types of BC including Neumann and Robin BC are excluded from this thesis.

Solution of System

Having went from the discrete system of equation to the reduced system, the system is now ready to be solved. The total number of DOFs can quite large ($\sim N = 2 \cdot N_z \cdot N_\theta \cdot N_\varphi$). The number of elements in the matrix A_{red} is therefore $\sim N^2$. Solving this system directly can quickly start to drain a lot of time. However, we observe that A and A_{red} are very sparse, therefore it is very efficient to use sparse matrix solver to solve our system. The open source linear algebra library, Eigen3 is used for this purpose. After comparing the performance of different available algorithms, we found that **SparseLU** (LU decomposition) gives us the best compromise between accuracy, stability and efficiency.

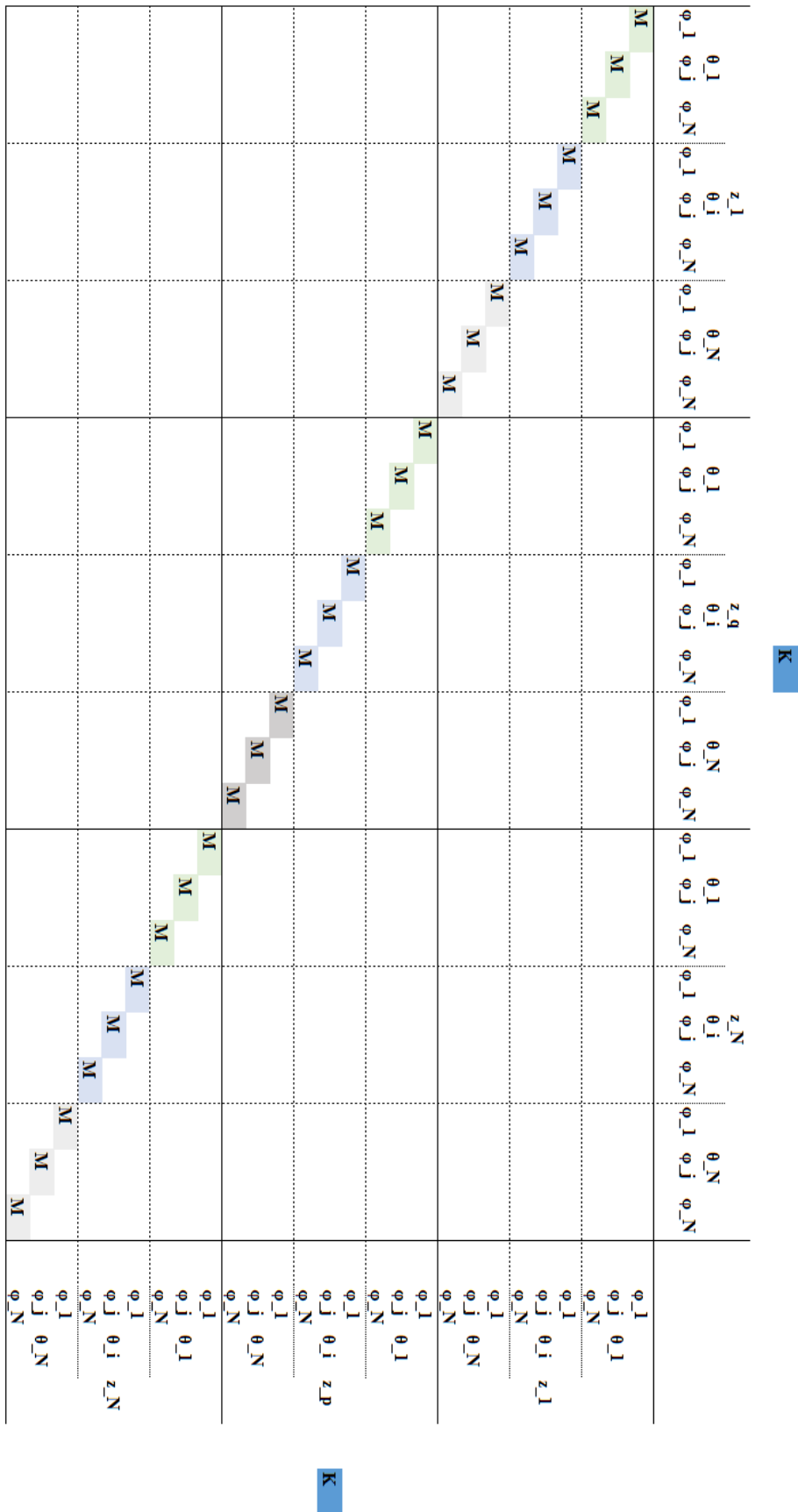


Figure 5.5: Schematic of Discrete Attenuation Coefficient

Chapter 6

Implementation

The simulation package is implemented as a collection of C++ classes. The final system of linear equations is solved using the external library Eigen3, which is the only dependency included in the simulation package besides the standard C++ libraries. The structure of the simulation package has been designed to maximize readability and maintainability, where functions are written to closely mirror the equations found in Chapter 5.

The different classes are organized according to the different components of the Generalized Darwin-Hamilton Equations. Each class is kept as encapsulated from each other as possible. The UI model has three levels of hierarchy as shown in Figure 6.1. At the top is the main function which allows the user to interact with the simulation package. The main function collects the appropriate input data and relay the necessary simulation parameters to `MatrixGen`. `MatrixGen` in turn is an aggregation of four classes: `ReflKern`, `ChebPoly`, `BoundCond`, and `MatrixSolver`. Figure 6.1 lists the representative public functions of each class.

In Figure 6.2, communication between classes are outlined. Figure 6.2 follows the logical flow of the simulation, listing functions in the order that they are run from top to bottom. Going from left to right, Figure 6.2 reflects the 3 different levels of encapsulations. The details of each of the forementioned classes are explained in the following subsections.

Matrix Generator

`main.cpp` communicates with `MatrixGen` via a Struct called `sim_parms`, which collects all the necessary input data, such as θ_B , N_z , N_θ , N_ϕ , etc. This Struct is passed to the `MatrixGen` constructor, which parses members of the Struct and calls the function `initialize`. This `initialize` function instantiates an object of each of the four classes `ReflKern`, `ChebPoly`, `BoundCond`, and `MatrixSolver` using the appropriate input parameters.

After initialization, three more functions are called, each reflecting a major step in the simulation process. The first function is `calc_matrix` where the reflection operator $R_{i,j,l,m}$, attenuation coefficient $M_{i,j}$ and differentiation matrix $D_{p,q}$ are calculated. The second function is `apply_dirichlet_BC` where the overall matrix A , and updated RHS $b_{updated}$ are assembled. The fourth function is `solve` where the Eigen3 libraries are called to solve the system of

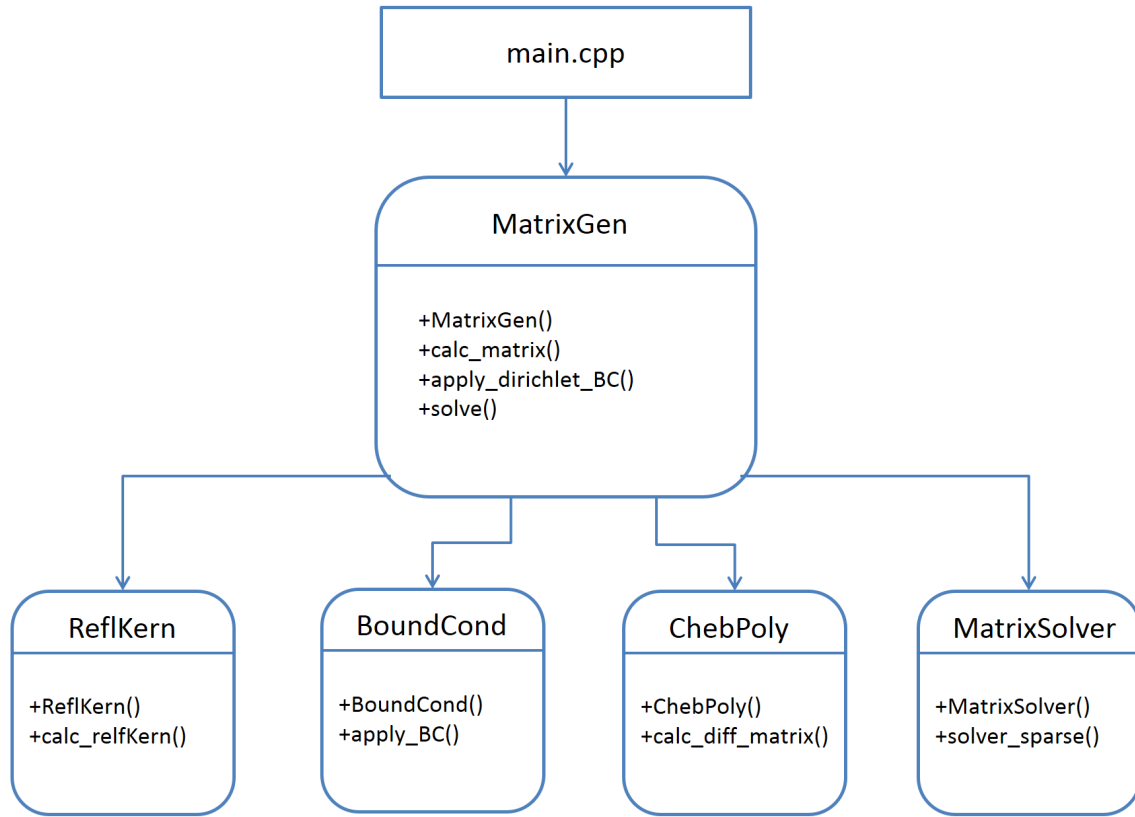


Figure 6.1: Schematic of Class Hierarchy

equations and the reflected and transmitted beams are calculated.

`MatrixGen` is responsible for maintaining discretization in θ , ϕ and z , while the classes underneath are oblivious to how these three variables are discretized.

Reflection Kernel

The class name `ReflKern` is short for Reflection Kernel. As the name suggests, the `ReflKern` class implements equations related to the reflection kern, which is a 4th order tensor. As explained in Chapter 5, this fourth order tensor is calculated as a list of triplets for each given \hat{k}^* . To this effect, `MatrixGen` communicates with `ReflKern` via the function `calc_reflKern`, which takes θ_i and ϕ_j as the input parameters, and returns the list of triplets (w, θ', ϕ') as a 2D array.

w representing the value of the integrand for each discrete β_p is given by function `integrand`, which implements Equation 5.5. The two angles θ' , ϕ' are calculated with helper functions `rotate_by_phi` and `spherical_unit_vector`, which represents the idea behind Equation 3.16.

For a given \hat{k}^* , the results of `calc_reflKern` is returned back to `MatrixGen` as a 2D array, $K_{i,j}(\beta_p)$. `MatrixGen` then takes $K_{i,j}(\beta_p)$ and transforms it into $K_{i,j}(\theta'_l, \phi'_m)$ as per Equation 5.6. Having obtained both $K_{i,j}(\beta_p)$ and $K_{i,j}(\theta'_l, \phi'_m)$, `MatrixGen` is able to calculate $R_{i,j,l,m}$

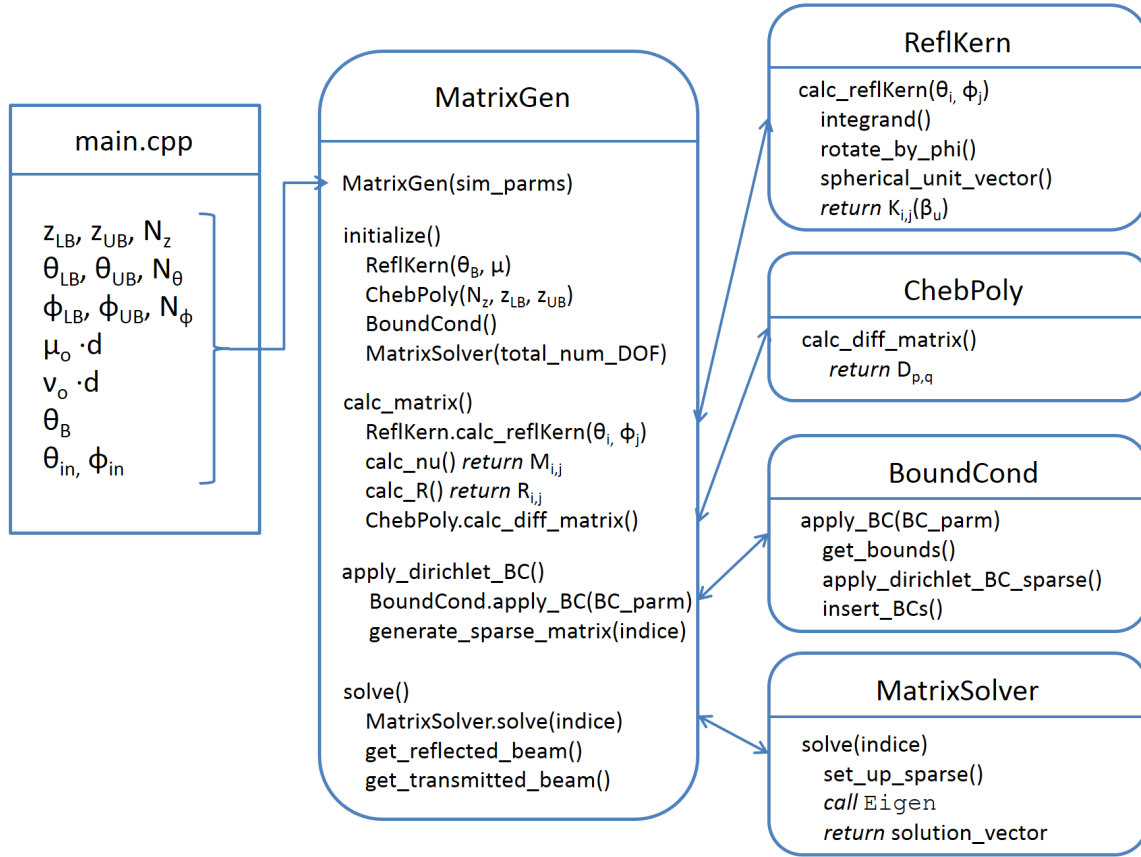


Figure 6.2: Communication between Classes

and $M_{i,j}$ as per Equations 5.18 and 5.9. The reflection operator $R_{i,j,l,m}$ and attenuation coefficients $M_{i,j}$ are given by functions `calc_nu` and `calc_R`.

Chebshv Polynomial

Another major component in the Generalized Darwin Hamilton equations is the differentiation matrix. The only input parameters necessary to generate this matrix are d and N_z , resolution of the discrete z variable. The class `ChebPoly` implements function called `calc_diff_matrix`, which calculates and returns $D_{p,q}$ according to Equations 5.16 and 5.17.

Boundary Condition

Having calculated the appropriate matrices, the overall matrix A and RHS $b_{updated}$ can be generated as per Equation 5.19. `MatrixGen` implements function `get_matrix_entry` which returns value in matrix A given by the row and column indice. `BoundCond` parses the information about the incoming boundary condition (Equation 3.3) and calculates $b_{updated}$. This requires discretization of mathematical description of $\psi_i(\hat{\mathbf{k}})$. Additionally, `BoundCond` also implements the transformation of A and $b_{updated}$ to the reduced system A_{red} and b_{red} through

the function `insert_BCs`. Functions `map_original` and `map_condensed` are used to map the indices of the full system to the reduced system and vice versa.

Matrix Solver

With A_{red} and b_{red} , the reduced system of equations can be solved to give us x_{red} . `MatrixSolver` implements the interface between the simulation package and the Eigen3 sparse matrix libraries. Using sparse matrix solvers lowers the memory requirement of the simulation package because the reduced system of equations contains a significant portion of zero entries. Sparse solvers also increases performance by speeding up the solution process.

After x_{red} is generated, post processing is performed to obtain the so-called transmitted beam and reflected beam via the functions `get_reflected_beam` and `get_transmitted_beam`. Definition of these two quantities are given by Equations 7.3 and 7.2.

Chapter 7

Results

In order to verify and validate the results of the numerical simulation, different calculations from the simulation package is compared against analytical solution and approximations found in literature. This chapter includes four different ways of checking the validity of the discrete system.

The first check is convergence in z against the analytical solution of the 1D Darwin Hamilton Equations. Analytical solution of the 1D equations is published by Sears [Sea97] and summarized in Appendix A. The second section compares the accuracy of discrete $\mu(\hat{\mathbf{k}})$ to the 1st and 2nd order approximations found in [Wut14]. The third section starts to look at the fully 3D results. θ and φ distribution of the reflected and transmitted beam are plotted. Also found in [Sea97] is plots of the effect of different Bragg reflectivity and attenuation coefficient on the reflected beam R . Similar plot is generated by the simulation package. Last section shows the so-called ‘rocking curves’, where reflected and transmitted beam are plotted for different incoming θ with all other parameters kept constant.

Before diving into the results, it is necessary to first define the following convention found in literature.

Incoming BC is generalized normalized, i.e.

$$\int \psi_i(\hat{\mathbf{k}}) d\hat{\mathbf{k}} := 1 \quad (7.1)$$

Furthermore, the incoming BC is commonly collimated, i.e., intensity is only non-zero at single θ_{in} and φ_{in} .

Results of interest include the so-called transmission

$$T := \int \psi_+(\hat{\mathbf{k}}, d) d\hat{\mathbf{k}} \quad (7.2)$$

and reflectivity

$$R := \int \psi_-(\hat{\mathbf{k}}, 0) d\hat{\mathbf{k}} \quad (7.3)$$

1D Darwin-Hamilton Equations

Looking at Appendix A, it appears that the analytical solution to the 1D Darwin-Hamilton Equations is easy to compute. To obtain the discrete solution is also rather straightforward where only $D_{p,q}$ needs to be calculated numerically. However there is one caveat that we have to keep in mind, which is the difference in notation between this thesis (following the convention at in [Wut14]) and [Sea97]. In this work, Bragg reflectivity is denoted by μ and attenuation coefficient by σ . In Sears, the opposite notation is used.

To study the accuracy of using the Chebyshev grid and corresponding differentiation matrix to approximate the 1D problem, the following results are presented.

For the 1D problem, three parameters need to be specified: Bragg reflectivity, attenuation coefficient, and ratio between θ_{in} and θ_B . The following plots are generated for Bragg reflectivity = 1.9, attenuation coefficient = 0.4 and $\theta_{in} = \theta_B = 45$ deg. For this set of parameters, the analytical solution is $R = 0.5185318175$ and $T = 0.1161138428$.

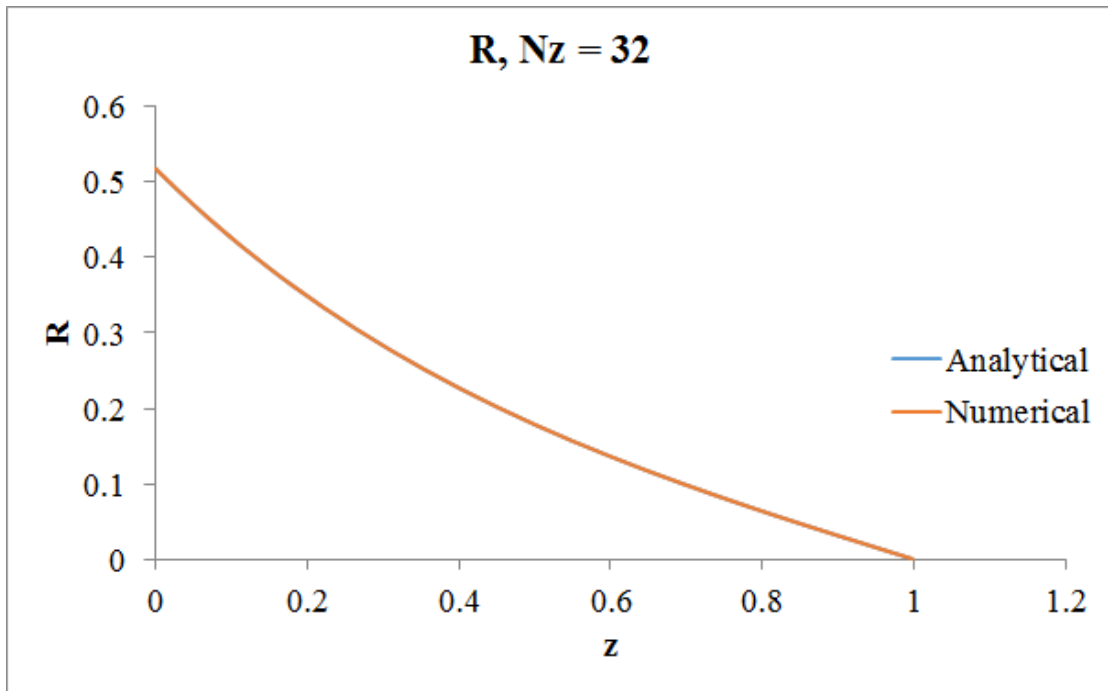


Figure 7.1: Plot of R as function z for $N_z = 32$

As seen in Figures 7.1 and 7.2, for $N_z = 32$, analytical and numerical results are almost identical. For a more detailed look into the accuracy of the numerical results, Figures 7.3 and 7.4 shows the respective relative error as function of z for $N_z = 32$. Relative error is defined as

$$rel.error = \text{abs}(numerical - analytical) / analytical \quad (7.4)$$

Indeed, $N_z = 32$ is too excessive for our problem, the relative error of R and T already drops to magnitude of 10^{-9} when $N_z = 8$. As the convergence plots in Figures 7.5 and 7.6 show,

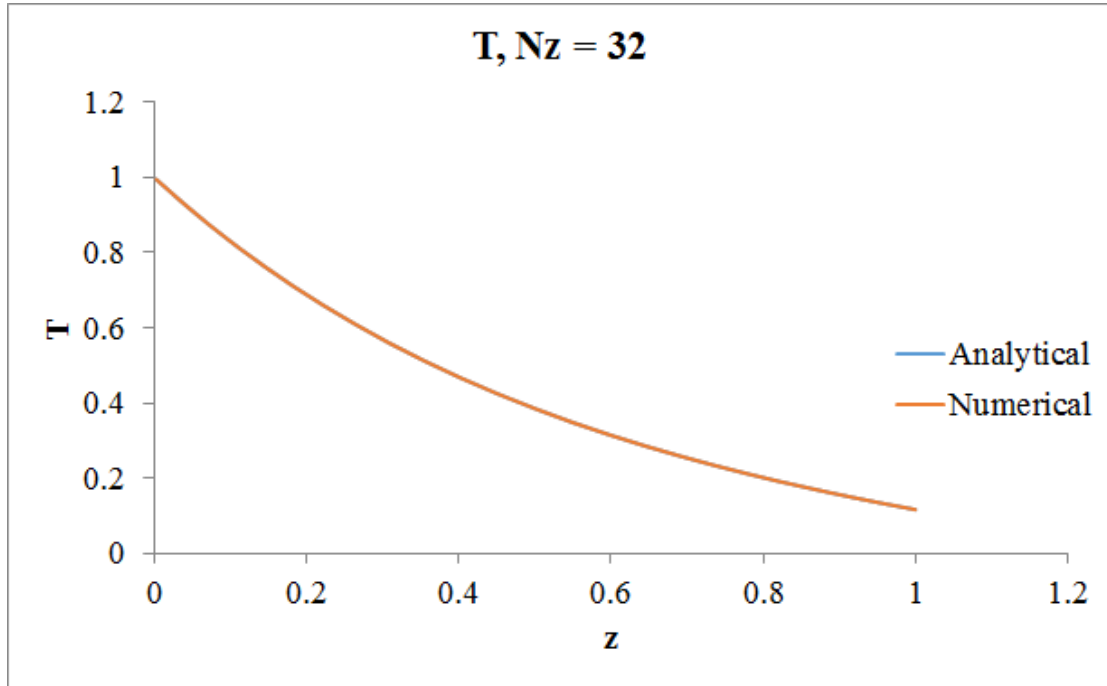


Figure 7.2: Plot of T as function z for $N_z = 32$

values of R and T flattens out after $N_z = 4$. This shows that spectral accuracy is achievable with Chebyshev polynomials for our 1D problem.

Discrete Bragg Reflectivity

Another part of the equation which can be checked against analytical results is the lineic Bragg reflectivity, $\mu(\hat{\mathbf{k}})$. Without repeating the derivation from [Wut14], $\mu(\hat{\mathbf{k}})$ is φ independent. First order approximation of μ is given by

$$\mu(\theta) \simeq \bar{\mu}G(\epsilon) \quad (7.5)$$

where $\epsilon = \theta - \theta_B$.

Second order approximation gives

$$\mu(\theta) \simeq \bar{\mu}\left(1 - \frac{\tan^2 \theta_B}{2}\eta^2\right)G\left(\epsilon - \frac{\tan^2 \theta_B}{2}\eta^2\right) \quad (7.6)$$

where η is the standard deviation of G .

To check the accuracy of the discrete formulation of μ , numerical results are compared against the two different approximations. Results of this comparison are simulated using the following parameters: $\eta = 0.025$ and $\bar{\mu} = 1.0$.

Figures 7.7 and 7.8 show the comparison of the three $\mu(\theta)$ for $\theta_B = 45$ deg and 80 deg. To

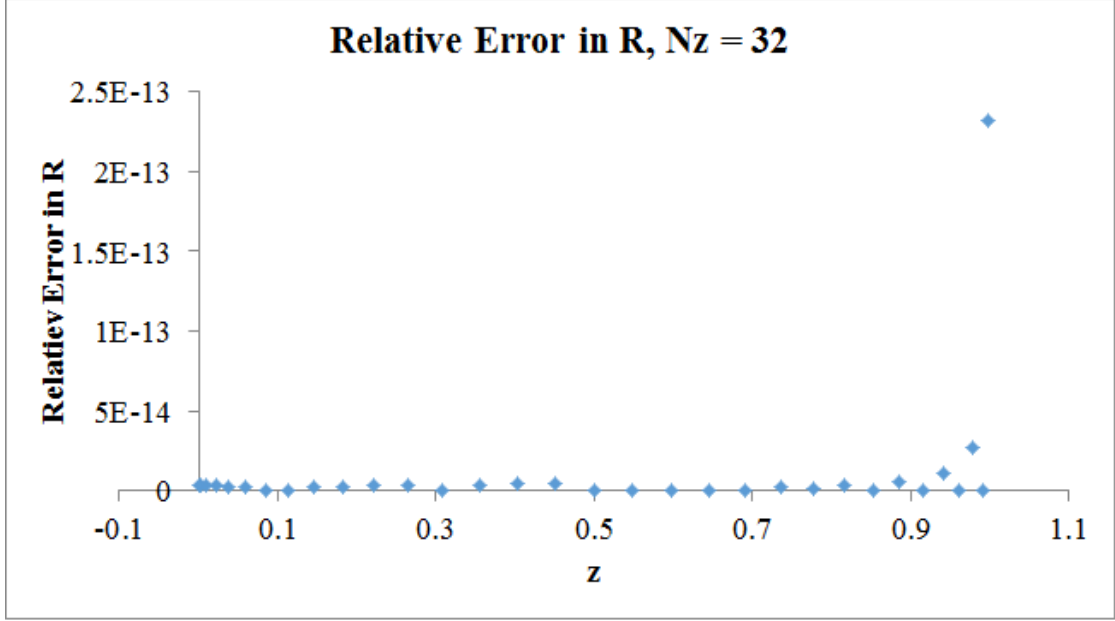


Figure 7.3: Plot of relative error in R as function z for $N_z = 32$

check the how μ converges with respect to N_β , Figures 7.9 and 7.10 show that value of μ flattens out after $N_\beta = 8$. For each convergence plot, the highest value of μ is used. For $\theta_B = 45$ deg, μ is maximized around $\theta = 45$ deg. Since only discrete values of θ are used, the closest discrete value is $\theta = 45.9000$. Similarly for $\theta_B = 80$ deg, the closest discrete value is $\theta = 80.1007$.

For $N_\beta = 8$, numerical results along with analytical approximations are listed in Table 7.1. One thing to note here is that even though $\mu(\theta)$ values converge for low N_β , higher N_β is used to give more accurate $\mu(\hat{\mathbf{k}}, \hat{\mathbf{k}}')$.

Table 7.1: Table of μ values from numerical simulation , 1st order, and 2nd order approximation

Angle (deg)	Numerical Result	First Order Apprx	Second Order Apprx
45	13.2045333786	13.099141638	13.1973027602
80	16.0393740037	15.9188636974	14.9490843956

Fully 3D results

To fully specify 3D results, we need to give the following parameters: Bragg reflectivity, attenuation coefficient, N_β , N_z , N_θ , N_ϕ , θ_{in} , ϕ_{in} , η and d . For the fully 3D problem, in keeping with [Wut14], Bragg reflectivity and attenuation are parameterized by $\tilde{\mu} = \frac{\bar{\mu}G(0)}{\sin \theta_{in}}$ and $\tilde{\varphi} = \frac{\phi}{\sin \theta_{in}}$. For the results listed in this section, value of parameters used listed in Table 7.2. Parameters not listed in the above table are specific to each study case.

One of the most intuitive way to check the validity of the results is to graphically visualize the solution vector. Quantities of interest are θ and φ distribution of R , which are defined below

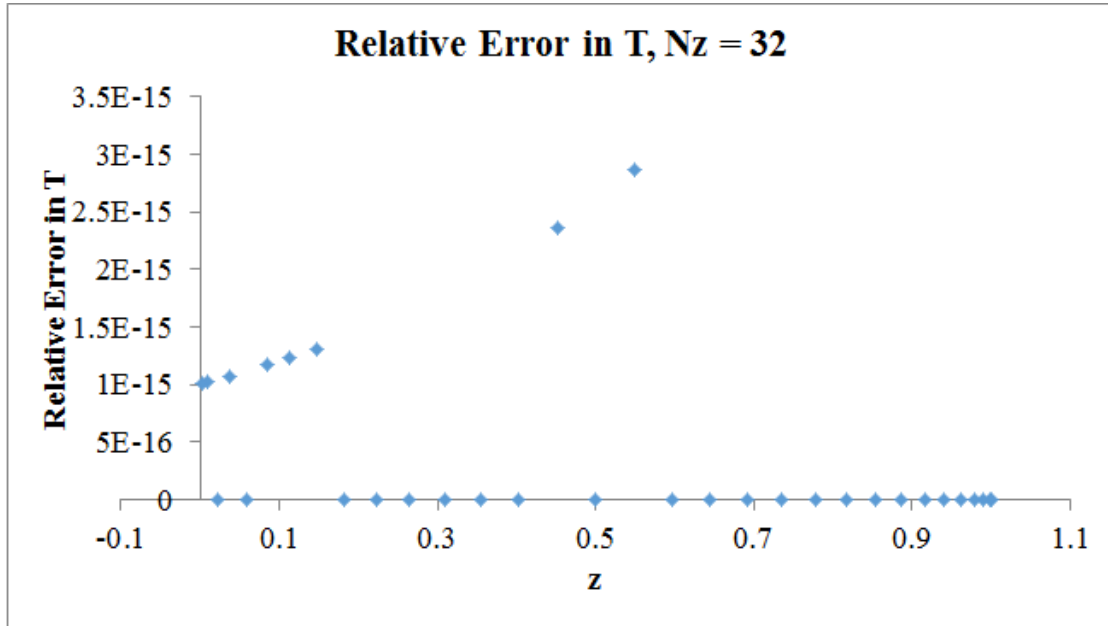


Figure 7.4: Plot of relative error in T as function z for $N_z = 32$

Table 7.2: List of parameters and corresponding value used in numerical simulation

Parameter	Value
N_β	1000
N_z	2
N_θ	50
N_ϕ	200
η	0.025
d	1.0

$$R(\theta) = \int \phi_-(\hat{\mathbf{k}}, 0) d\varphi \quad (7.7)$$

$$R(\phi) = \int \phi_-(\hat{\mathbf{k}}, 0) d\theta \quad (7.8)$$

Similar definition hold for T .

Figures 7.11 to 7.14 show plots of $R(\theta)$, $R(\varphi)$, $T(\theta)$, and $T(\varphi)$ for $\theta_B = \theta_{in} = 80$ deg, $\tilde{\mu} = 1.0$, and $\tilde{\sigma} = 0.0$. Compared to Figures 13 from [Wut14] resulting from Monte Carlo simulation, Figures 7.11 shows similar pattern in $R(\theta)$ with peak at $\theta = \theta_B$ and rapid decline away from θ_B . However, Figure 7.13 shows significant deviation from Figure 12 from [Wut14] (results from Monte Carlo simulation and analytical approximation), and what appears to be numerical instability around $\theta = 90$ deg and $\theta = 180$ deg. $T(\theta)$ and $T(\phi)$ are shown without comparable results found in literature.

Figures 7.15 to 7.18 show plots of $R(\theta)$, $R(\varphi)$, $T(\theta)$, and $T(\varphi)$ for $\theta_B = \theta_{in} = 45$ deg. $\tilde{\mu} = 1.0$ and $\tilde{\sigma} = 0.0$. In figure 7.15 and 7.16, magnitude peaks around 45 deg and not directly at

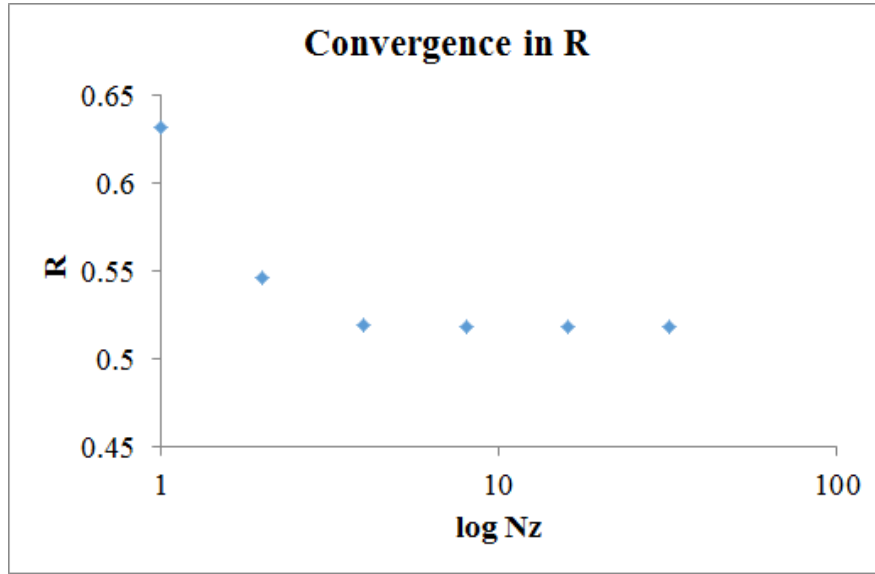


Figure 7.5: Plot of convergence in R as function N_z

45 deg. This could be an effect from the coarse discretization in θ where $\Delta\theta = 1.9$ deg.

Effect of Bragg Reflectivity and Attenuation Coefficient

In Figure 3 from [Sea97], R is plotted as a function of Bragg reflectivity and attenuation. Although there is no one to one equivalence mapping Sears' parameters b, a to our $\tilde{\mu}, \tilde{\sigma}$, both $\tilde{\mu}$ and b correspond to Bragg reflectivity; and both $\tilde{\sigma}$ and a correspond to attenuation.

Comparing Figure 3 from [Sea97] to Figure 7.19, we can observe similarity in the pattern of R as function of Bragg reflectivity and attenuation. There is an exponential increase in R with increase in Bragg reflectivity. There is also decrease in R curve when attenuation is increased.

Rocking Curves

One common technique used in neutron diffraction generates the so-called rocking curves where θ_B is kept constant while the crystal slab rotates around an axis, thereby changing θ_{in} . Figure 10 from [Wut14] shows the rocking curve for $\theta_B = 45$ deg and 80 deg. For both θ_B , R shows peak around θ_B , and T shows a valley. In Figures 7.20 to 7.22, the rocking curves for $\theta_B = 45$ deg generated by the simulation package are shown. In Figures 7.23 to 7.25, the rocking curves for $\theta_B = 80$ deg is shown.

From both set of rocking curves generated by the simulation package, we can observe the peak in R and the valley in T around θ_B . From [Wut14], the peak in R is shown to be shifted from $\theta_{in} = 80$ deg to $\theta_{in} = 80.5$ deg. This shift is hard to observe in the numerical simulation where discretization is coarse ($\Delta\theta = 1.8$ deg). There are two more noticeable differences between the our numerical simulation and results found in [Wut14]. Firstly, the magnitude of R from numerical simulation (10^{-4}) is very low in comparison to the results given in [Wut14] (10^{-1}).

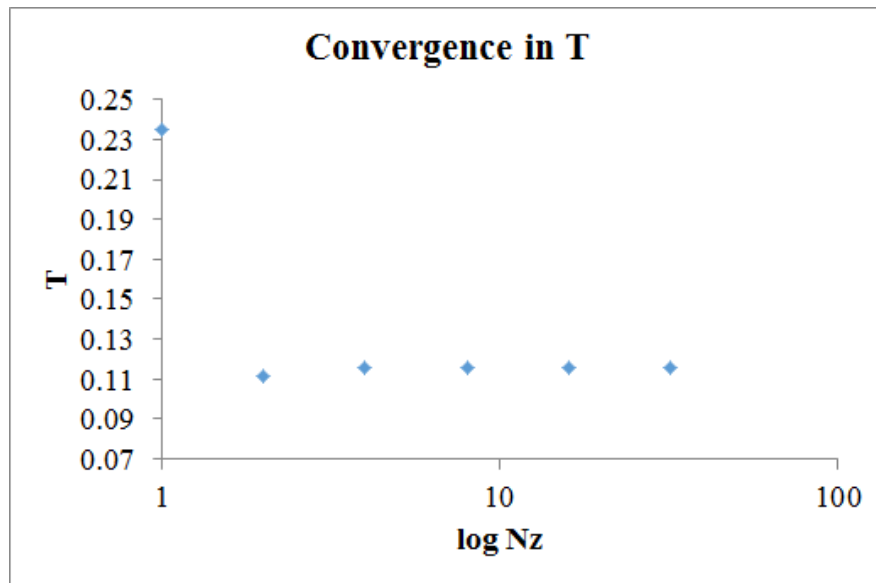


Figure 7.6: Plot of convergence in T as function N_z

Secondly, in [Wut14] $1 - R - T$ dips around θ_B while Figures 7.22 and 7.25 show peak in $1 - R - T$ around θ_B .

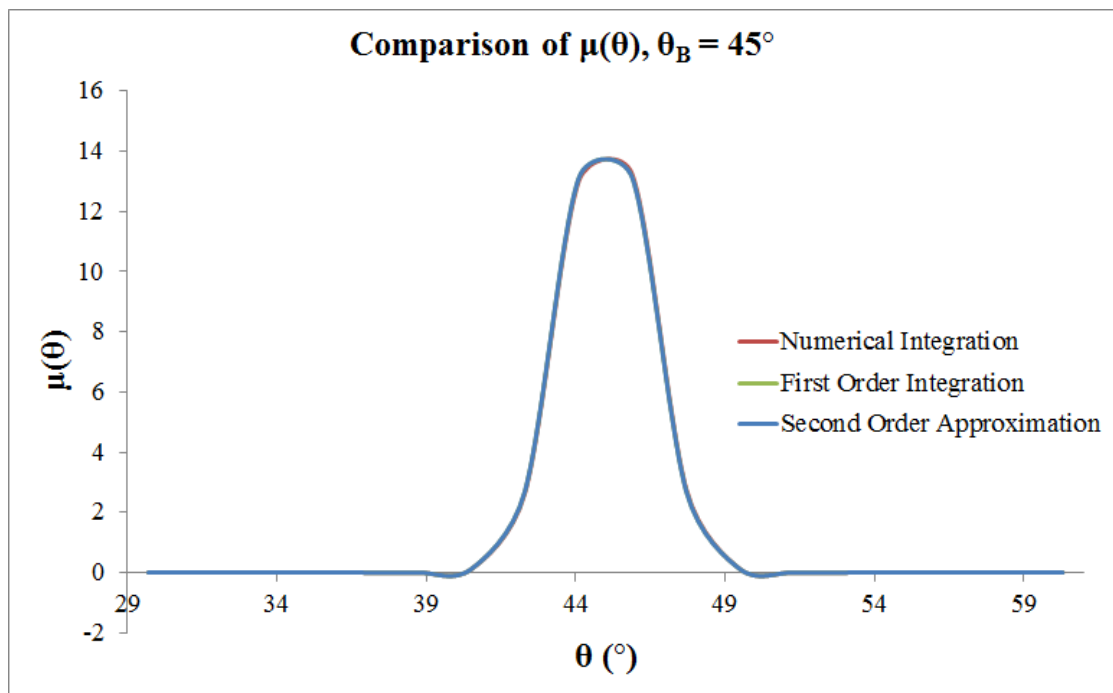


Figure 7.7: Comparison of μ as function θ for $\theta_B = 45$ deg

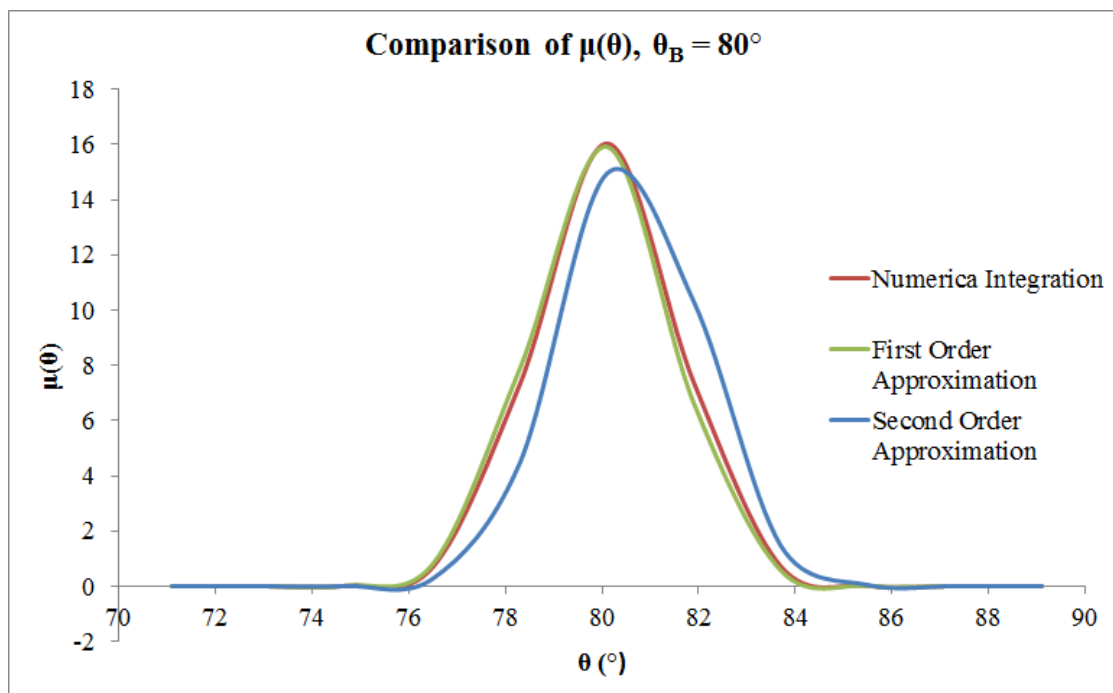


Figure 7.8: Comparison of μ as function θ for $\theta_B = 80$ deg

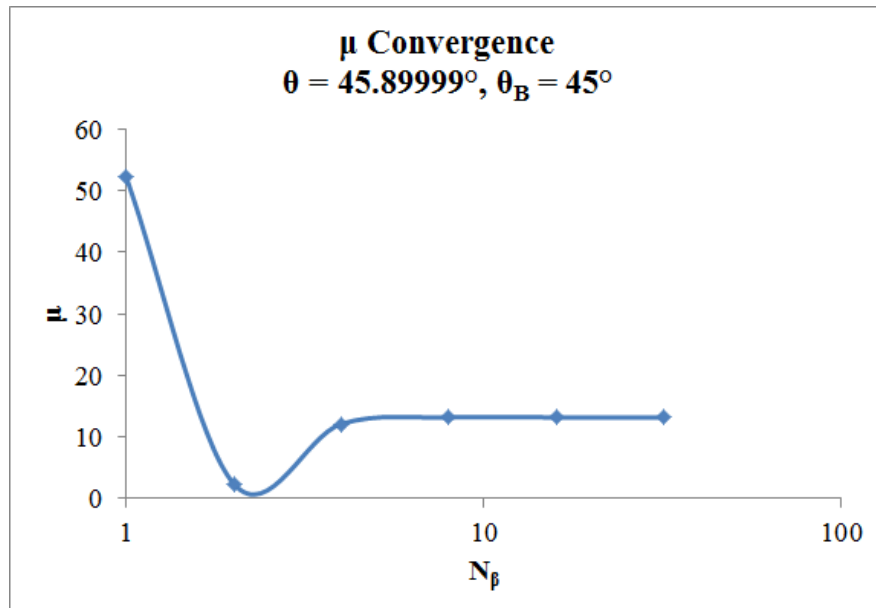


Figure 7.9: Convergence of $\mu(\theta = 45.9000)$ as function N_β for $\theta_B = 45$ deg

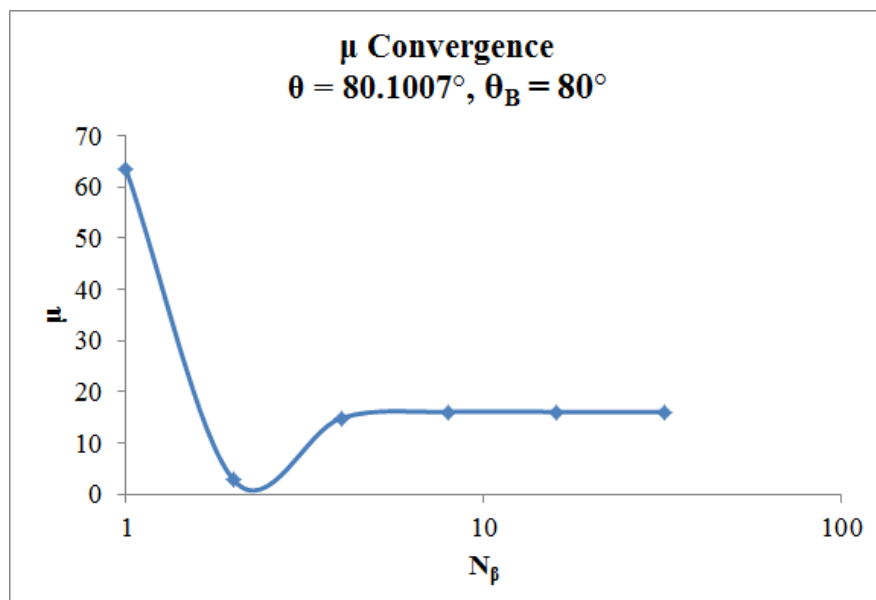
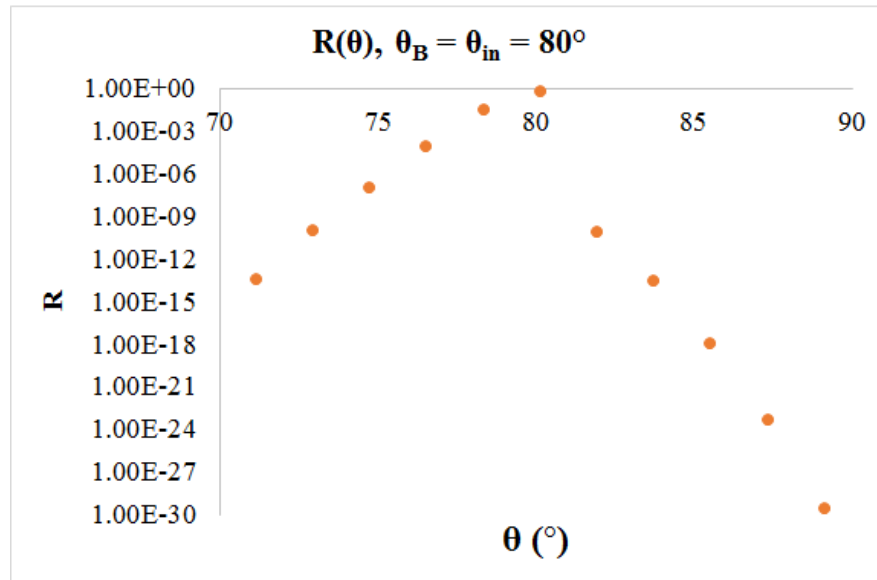
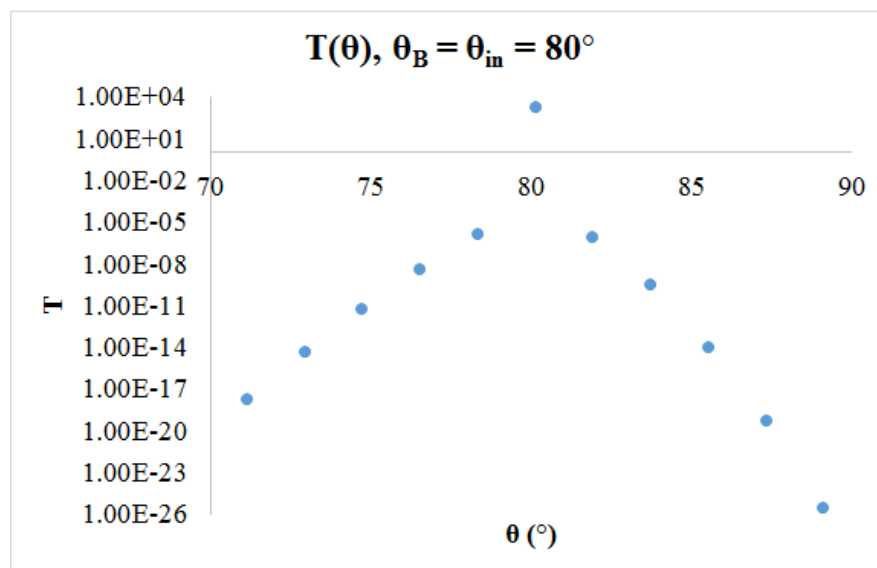


Figure 7.10: Convergence of $\mu(\theta = 80.1007)$ as function N_β for $\theta_B = 80$ deg

Figure 7.11: $R(\theta)$ for $\theta_B = \theta_{in} = 80$ degFigure 7.12: $T(\theta)$ for $\theta_B = \theta_{in} = 80$ deg

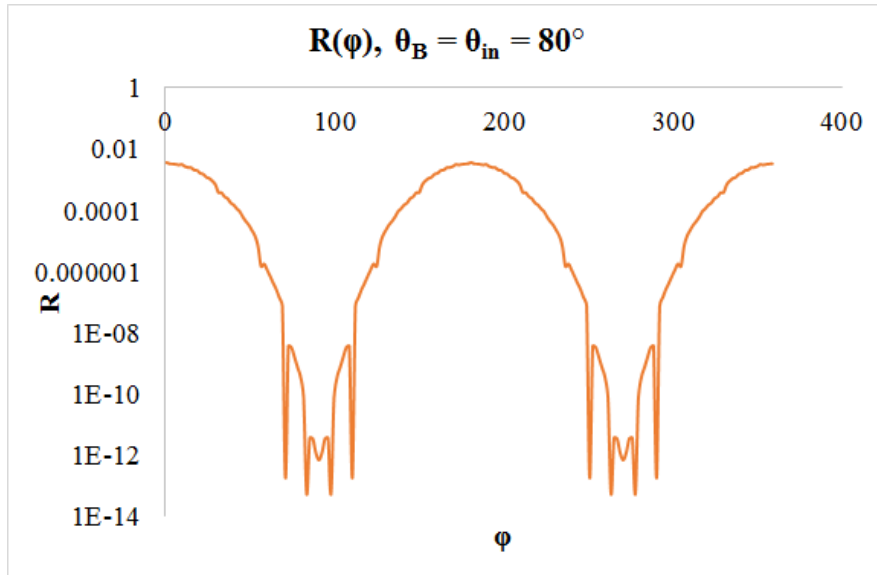


Figure 7.13: $R(\phi)$ for $\theta_B = \theta_{in} = 80$ deg

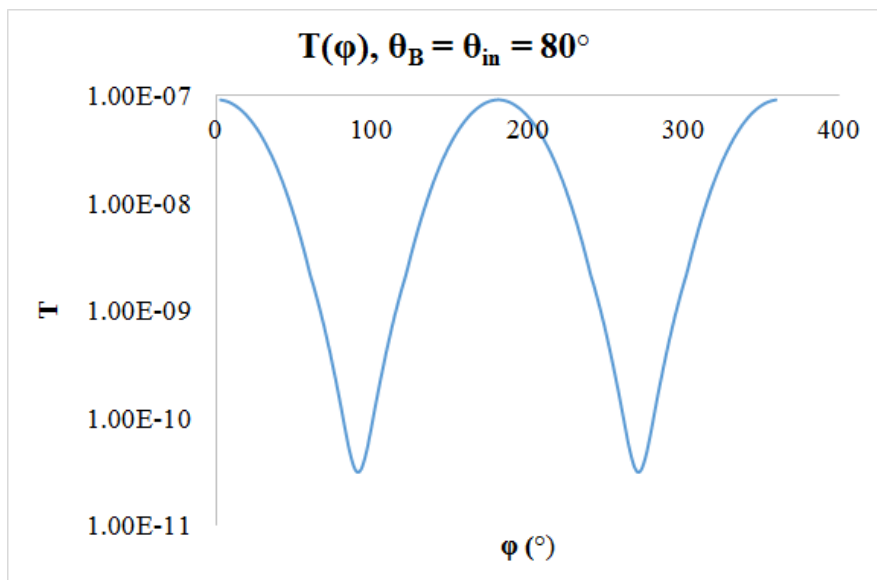
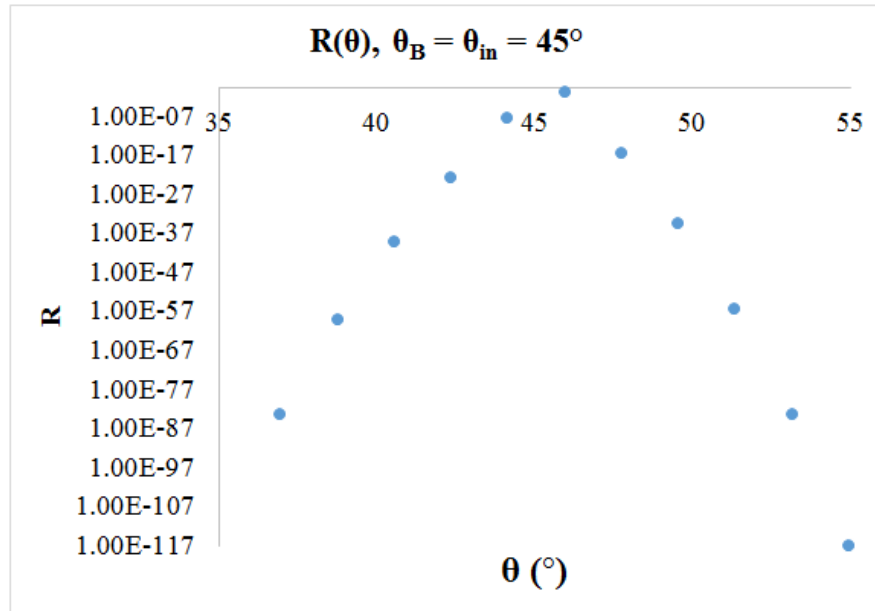
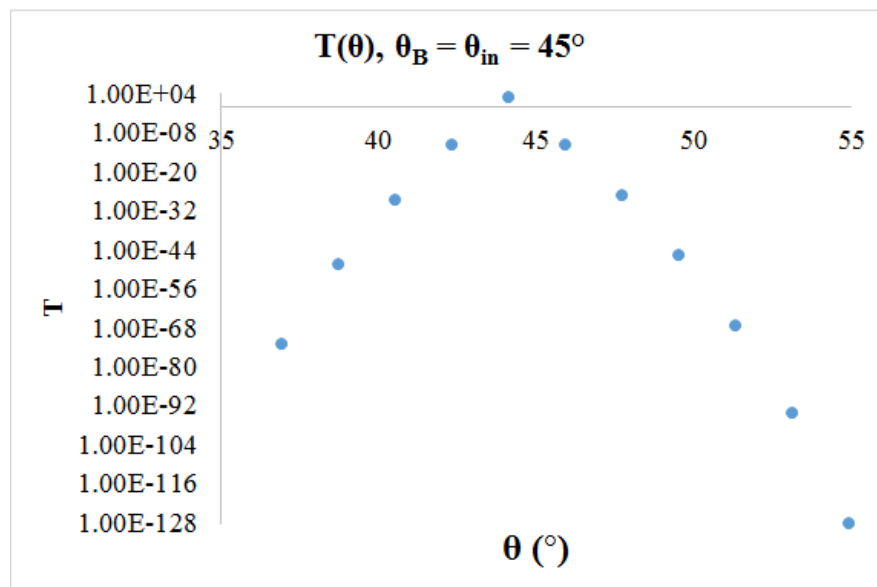


Figure 7.14: $T(\phi)$ for $\theta_B = \theta_{in} = 80$ deg

Figure 7.15: $R(\theta)$ for $\theta_B = \theta_{in} = 45$ degFigure 7.16: $T(\theta)$ for $\theta_B = \theta_{in} = 45$ deg

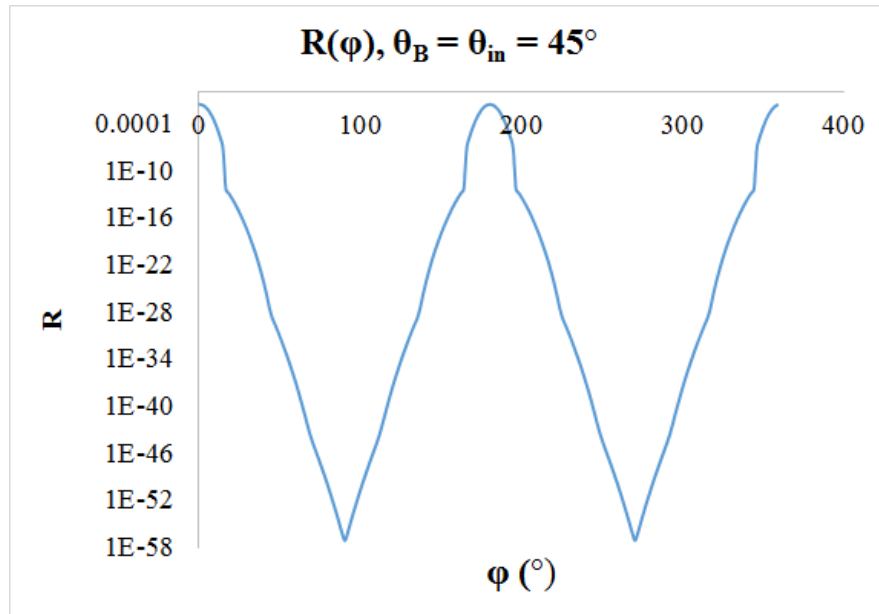


Figure 7.17: $R(\phi)$ for $\theta_B = \theta_{in} = 45$ deg

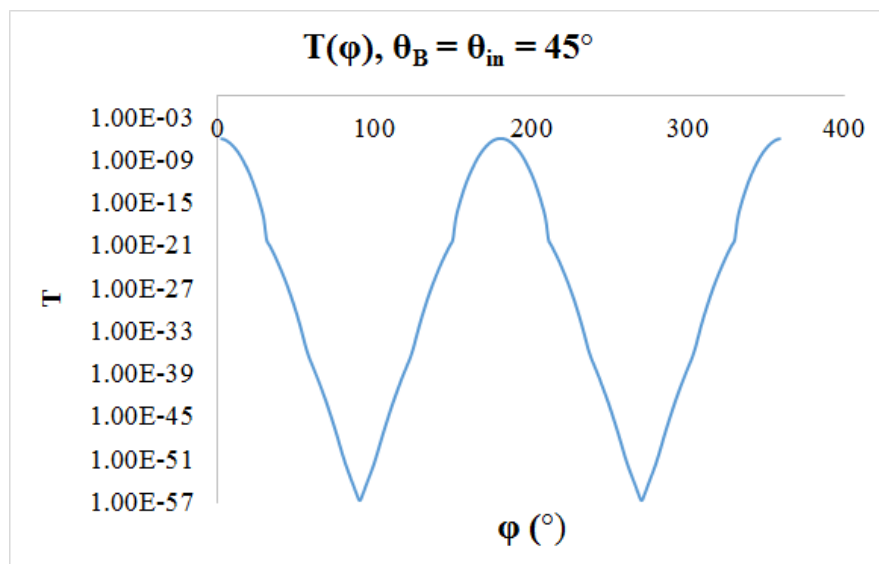


Figure 7.18: $T(\phi)$ for $\theta_B = \theta_{in} = 45$ deg

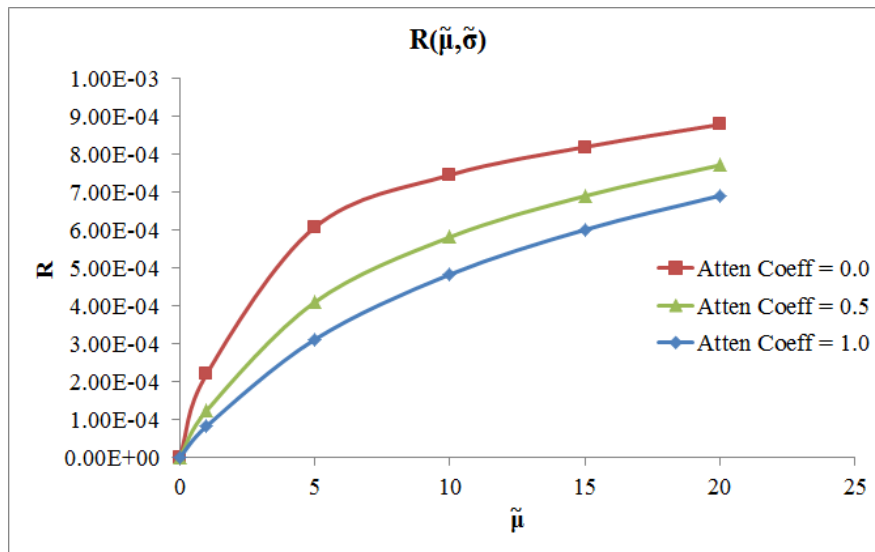


Figure 7.19: R as function of μ and σ for $\theta_B = \theta_{in} = 45$ deg

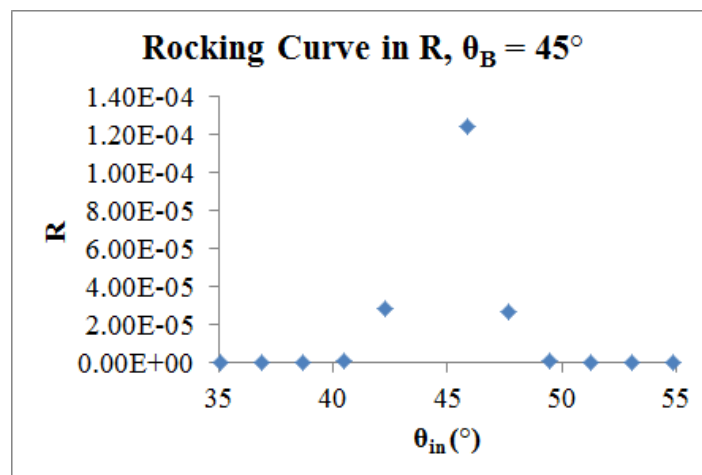


Figure 7.20: Rocking Curve - R, $\theta_B = 45$ deg

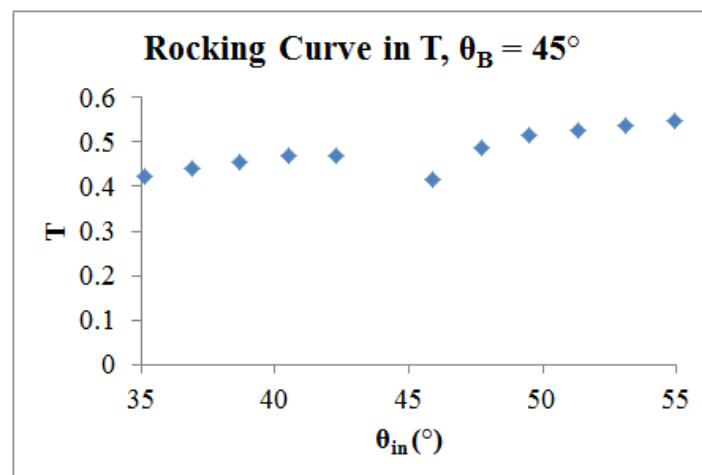


Figure 7.21: Rocking Curve - T, $\theta_B = 45$ deg

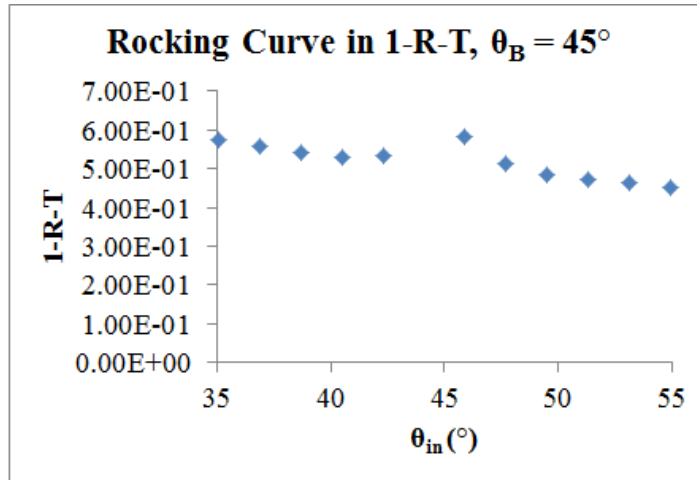


Figure 7.22: Rocking Curve - 1 - R - T, $\theta_B = 45$ deg

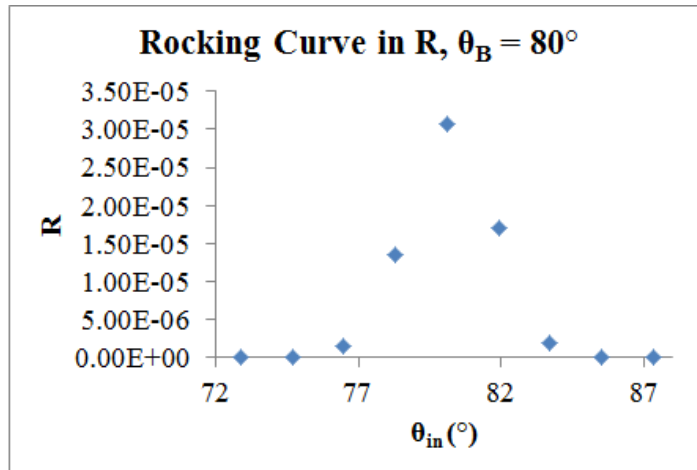


Figure 7.23: Rocking Curve - R, $\theta_B = 80$ deg

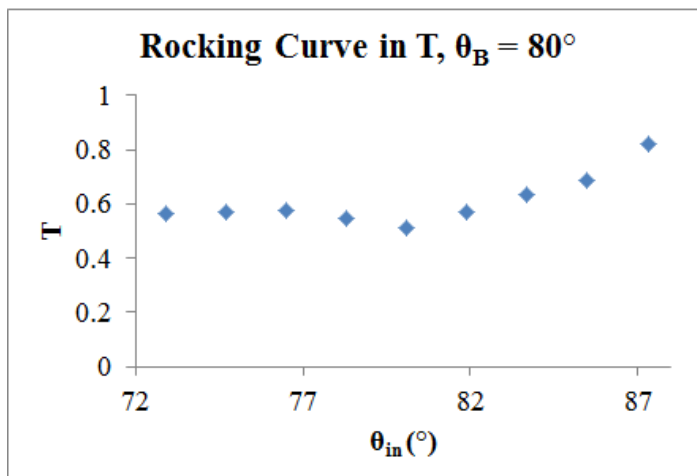


Figure 7.24: Rocking Curve - T, $\theta_B = 80$ deg

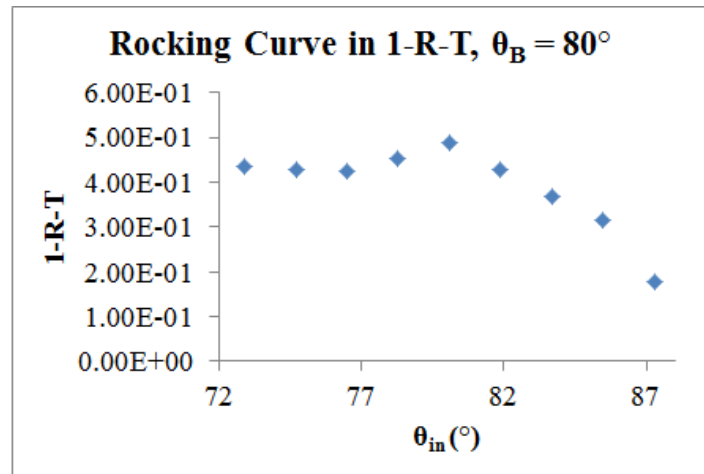


Figure 7.25: Rocking Curve - 1 - R - T, $\theta_B = 80$ deg

Chapter 8

Conclusion

In this thesis, the overall objective is to simulate the physical phenomenon of multiple Bragg reflection inside a mosaic crystal using the spectral method. In order to achieve this goal, the first step was to establish a firm understanding of the physics behind multiple Bragg reflection with the different mathematical models found in literature, and to study the principles behind spectral methods. Next, the appropriate mathematical model was translated into discrete equations using rectangular discretization in the polar and azimuthal angles and Chebyshev grid in z . At the same time, a stand alone simulation package is developed in C++ to implement the discrete equations and to verify the validity of the discrete equations.

As shown in Figure 1.1, there are three different types of systematic error when we try to simulate a physical system with discrete solution. The errors can come from idealization (modeling), discretization, and/or the solution step. Solution error results from the fact that computers have round off errors and linear algebra algorithms can have definite accuracy. This source of error is the easiest to quantify. To study this type of error, $norm(A.x - b)/norm(b)$ is taken. For simulations using parameters established in Table 7.2, the order of solution error are in the range of 10^{-15} to 10^{-16} .

It can be more difficult to quantify and separate modeling and discretization errors. Modeling error results from simplifications and assumptions used in the mathematical model in order to capture the physics in a meaningful and solvable way. Discretization error results from definite accuracy of the numerical methods. For this thesis, results are mainly verified against results found in literature ([Sea97] and [Wut14]). In the 1D case, Chebyshev discretization scheme is proven to converge to the analytical solution found in [Sea97] relatively fast.

For the fully 3D problem, results are mainly verified against monte carlo simulation and analytical approximations found in [Wut14]. As a first attempt at discretizing the 3D generalized Darwin-Hamilton Equations, results from the numerical simulation are mixed. Looking at Chapter 7, most patterns found in solution of the numerical simulations tend to agree with predictions found in literature. For calculation of lineic Bragg reflectivity, numerical integration converges quickly to predictions found in [Wut14]. Further validation of results is done by comparing various graphs. The so-called reflected and transmitted beam are plotted in θ and ϕ . For the reflected beam, θ distribution agrees with predictions found in [Wut14] while ϕ distribution does not. Numerically simulated reflected beam as function of Bragg

reflectivity and attenuation coefficient also agrees with analytical prediction [Sea97]. As for the rocking curves, general trend of both reflected beam and transmitted beam as function of incoming boundary condition also agree with predictions found in [Wut14].

The worst discrepancy found between simulated numerical solution and predictions found in literature is the magnitude of the reflected beam, which is several magnitude smaller than predicted values. This indicates that further investigation is still necessary to find out precisely if this is due to human error, discretization error or modeling error. This also leads naturally to areas of possible improvements.

Firstly, a straightforward discretization of θ and ϕ is used in this thesis, which may not be the most efficient method. For our system of equations, the number of DOFs can quickly add up. For simulations parameterized by Table 7.2, $N_{DOF} = 2 \cdot (2 + 1) \cdot 200 \cdot 50 = 60000$, while discretization in the two angles are still rather coarse ($\Delta\theta = \Delta\phi = 1.9$ deg). With the current discretization scheme, memory and performance can easily become a limiting factor for increasing the level of refinement of our discrete grid. Having a more refined grid can enable us to discern whether discrepancies are due to discretization error. Secondly, efforts to debug and check the simulation package have been limited to two literature sources. It may be helpful to also look directly at experimental data generated by real monochromators used in neutron research centers.

In summary, significant progress have been made in the duration of this thesis with many lessons learnt, and some open questions left to be explored.

Appendix A

Crystalline Structure

This section aims to give a brief introduction into the description of crystalline structure, Bragg planes and to offer a schematic on a type of crystal imperfection, dislocation, which has been used to explain mosaicity in crystals. The content of this appendix can be found in many different introductory solid state physics textbooks. The notation in this appendix follows the notation used in [Sea89].

A perfect crystal contains periodic arrangement of the same group of atoms. To fully specify the structure of a crystal, it is necessary to first specify internal arrangement of the repeated group of atoms, which is known as the unit cell. The key property of a perfect crystal is that all unit cells found in the crystal are identical.

To fully specify a unit cell, it is necessary to give the chemical species and spatial coordinates of each atom in the unit cell. The interested reader can refer to [N.W76] and [Sea89] for descriptions of common crystal structures. For a given atom, the spatial coordinates (x, y, z) can be given as a set orthogonal unit vector $(\mathbf{a}, \mathbf{b}, \mathbf{c})$

$$\mathbf{r}_v = x\mathbf{a} + y\mathbf{b} + z\mathbf{c} \quad (\text{A.1})$$

The second item needed to fully specify the crystal is the space lattice, i.e. how the unit cells are arranged in space with respect to each other. A space lattice is a period array of points in space, where each point is also called lattice sites and l th site is given by the lattice vector

$$\mathbf{R}_l = l_1\mathbf{a}_1 + l_2\mathbf{a}_2 + l_3\mathbf{a}_3 \quad (\text{A.2})$$

Here $\mathbf{a}_1, \mathbf{a}_2, \mathbf{a}_3$ are non-coplanar translation vectors and $l_1, l_2, l_3 = 0, \pm 1, \pm 2 + \dots$. The most types of lattices are cubic and hexagonal.

The position of the v th atom in the l th unit cell is given by

$$\mathbf{r}_{lv} = \mathbf{R}_l + \mathbf{r}_v \quad (\text{A.3})$$

Bragg Planes

Each lattice in \mathbf{r} space has a unique corresponding reciprocal lattice in \mathbf{k} space. The h th reciprocal lattice site is given by three reciprocal lattice vectors

$$\mathbf{K}_h = h_1 \mathbf{b}_1 + h_2 \mathbf{b}_2 + h_3 \mathbf{b}_3 \quad (\text{A.4})$$

where

$$\mathbf{b}_i = \frac{2\pi}{V_o} \mathbf{a}_j \times \mathbf{a}_k \quad (\text{A.5})$$

for $i \neq j \neq k$. And V_o is the volume of the unit cell ($a_1 \cdot a_2 \times a_3$)

This gives the result that $e^{i\mathbf{K}_h \mathbf{R}_l} = 1$ for all h and l . Bragg planes results from this definition of the reciprocal lattice vectors. Each \mathbf{K}_h in \mathbf{k} space divides the lattice sites in \mathbf{r} space into a set of equally spaced, parallel planes, i.e. Bragg planes. These planes are orthogonal to \mathbf{K}_h and are separated by $d_h = \frac{2\pi n}{K_h}$. This d_h is the inter-planar distance in the Bragg condition in Equation 2.1. [Sea97]

Dislocation

Among the different possible types of imperfection that can found in a crystal, dislocation is what gives rise to mosaicity. In a carefully annealed single crystal, dislocation generally form in semi-parallel, equally spaced lines. This effectively partitions the crystal into a number of mosaic block where each block is a perfect crystal, displaced and misoriented with respect to its neighbours.

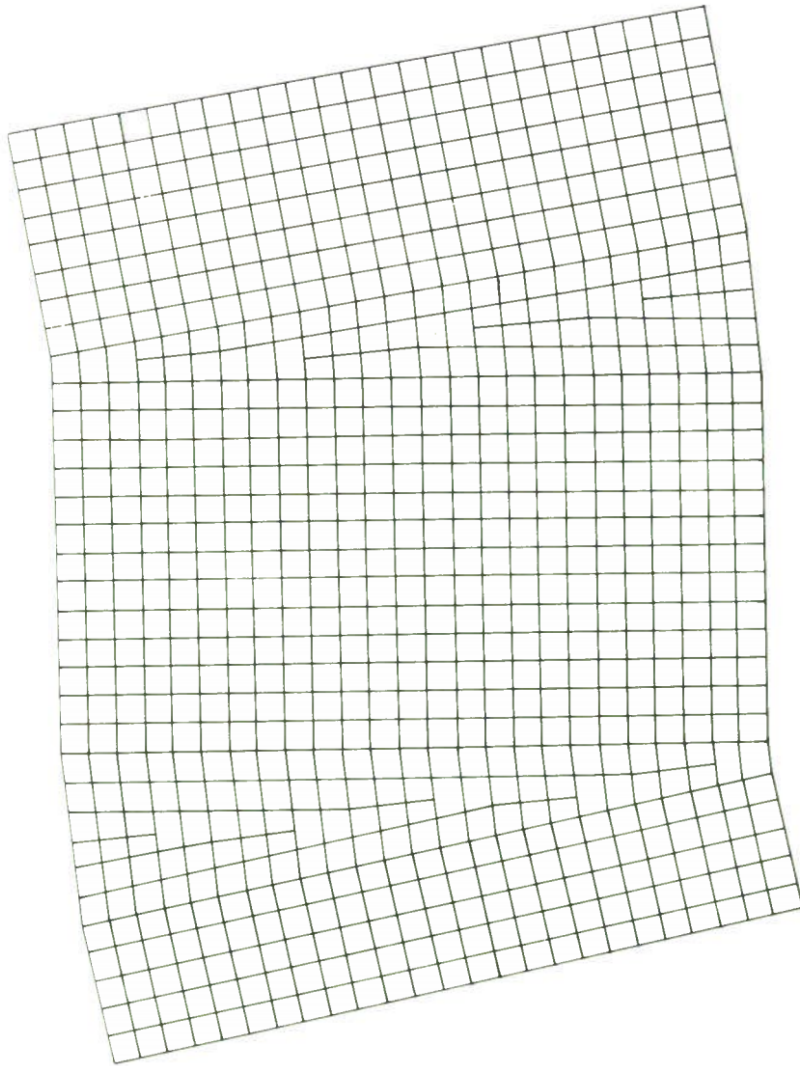


Figure A.1: Schematic of mosaic crystal with edge dislocation
[Sea97]

Appendix B

Analytical Solution by Sears

Published in 1997, Sears used Mathematica to derive the analytical solution to the original 1D Darwin-Hamilton equation where both incident beam and reflected beam are restricted to be in-plane, and only one $\hat{\mathbf{k}}_-$ is possible. For his simplified formulation of the multi reflection problem, the governing equation is given by two equations below

$$(\partial_z + \alpha + \beta)I(z) = \beta'I'(z) \quad (\text{B.1})$$

$$(-\partial_z + \alpha' + \beta')I'(z) = \beta I(z) \quad (\text{B.2})$$

where

$$\alpha = \frac{\mu}{\sin\theta} \quad \beta = \frac{\sigma}{\sin\theta}$$

$$\alpha' = \frac{\mu}{\sin\theta'} \quad \beta' = \frac{\sigma}{\sin\theta'}$$

The analytical solution is obtained for the following set of boundary conditions:

$$I(0) = 1 \quad I'(d) = 0 \quad (\text{B.3})$$

Let

$$a = \alpha d \quad b = \beta d \quad \zeta = \frac{\sin\theta}{\sin\theta'}$$

And

$$p = (a + b)(1 + \zeta)/2 \quad q = (a + b)(1 - \zeta)/2$$

$$r = (p^2 - \zeta b^2)^{1/2} \quad s = (p^2 + \zeta b^2)^{1/2}$$

Finally, intensities of incident and diffracted beams are given by the two equations below.

$$I(z) = e^{-qz/d} \frac{r \cosh[r(1-z)] + p \sinh[r(1-z)]}{r \cosh r + p \sinh r} \quad (\text{B.4})$$

$$I'(z) = e^{-qz/d} \frac{b \sinh[r(1-z)]}{r \cosh r + p \sinh r} \quad (\text{B.5})$$

The quantities of special interest are $T = I(z = d)$ and $R = I'(z = 0)$. The analytical solution for R and T are given by.

$$R = \frac{b}{r \coth r + p \sinh r} \quad (\text{B.6})$$

$$T = \frac{r e^{-q}}{r \cosh r + p \sinh r} \quad (\text{B.7})$$

List of Figures

1.1	Main stages of computer-based simulation [Fel]	3
2.1	Illustration of Two Slit Diffraction Pattern [Rot03]	4
2.2	Illustration of Bragg Reflection [N.W76]	6
2.3	Schematic of geometry used in boundary value problem	7
2.4	Schematic of multiple reflection inside a perfect crystal	8
3.1	Schematic of geometry used in boundary value problem [Wut14]	13
4.1	Schematic of the First Chebyshev Differentiation Matrix [Tre01]	23
5.1	Schematic of converting $K_{i,j}(\beta_u)$ to $K_{i,j}(\theta'_l, \varphi'_m)$	26
5.2	Chebyshev points on $[-1, 1]$ [Tre01]	28
5.3	Schematic of A and x	29
5.4	Schematic of solution vector x	30
5.5	Schematic of Discrete Attenuation Coefficient	32
5.6	Schematic of Discrete Reflection Operator	33
5.7	Schematic of Differentiation Matrix	34
5.8	Schematic of Reduced System of Equations	35
6.1	Schematic of Class Hierarchy	37
6.2	Communication between Classes	38
7.1	Plot of R as function z for $N_z = 32$	41
7.2	Plot of T as function z for $N_z = 32$	42
7.3	Plot of relative error in R as function z for $N_z = 32$	43

7.4	Plot of relative error in T as function z for $N_z = 32$	44
7.5	Plot of convergence in R as function N_z	45
7.6	Plot of convergence in T as function N_z	46
7.7	Comparison of μ as function θ for $\theta_B = 45$ deg	47
7.8	Comparison of μ as function θ for $\theta_B = 80$ deg	47
7.9	Convergence of $\mu(\theta = 45.9000)$ as function N_β for $\theta_B = 45$ deg	48
7.10	Convergence of $\mu(\theta = 80.1007)$ as function N_β for $\theta_B = 80$ deg	48
7.11	$R(\theta)$ for $\theta_B = \theta_{in} = 80$ deg	49
7.12	$T(\theta)$ for $\theta_B = \theta_{in} = 80$ deg	49
7.13	$R(\phi)$ for $\theta_B = \theta_{in} = 80$ deg	50
7.14	$T(\phi)$ for $\theta_B = \theta_{in} = 80$ deg	50
7.15	$R(\theta)$ for $\theta_B = \theta_{in} = 45$ deg	51
7.16	$T(\theta)$ for $\theta_B = \theta_{in} = 45$ deg	51
7.17	$R(\phi)$ for $\theta_B = \theta_{in} = 45$ deg	52
7.18	$T(\phi)$ for $\theta_B = \theta_{in} = 45$ deg	52
7.19	R as function of μ and σ for $\theta_B = \theta_{in} = 45$ deg	53
7.20	Rocking Curve - R , $\theta_B = 45$ deg	53
7.21	Rocking Curve - T , $\theta_B = 45$ deg	53
7.22	Rocking Curve - $1 - R - T$, $\theta_B = 45$ deg	54
7.23	Rocking Curve - R , $\theta_B = 80$ deg	54
7.24	Rocking Curve - T , $\theta_B = 80$ deg	54
7.25	Rocking Curve - $1 - R - T$, $\theta_B = 80$ deg	55
A.1	Schematic of mosaic crystal with edge dislocation	60

List of Tables

7.1	Table of μ values from numerical simulation , 1st order, and 2nd order approximation	43
7.2	List of parameters and corresponding value used in numerical simulation . . .	44

Bibliography

- [C.C06] C.Canuto, M.Y.Hussaini, A.Quarteroni and T.A.Zang. *Spectral Methods: Fundamentals in Single Domains*. Springer-Verlag Berlin Heidelberg, 2006.
- [F.B] F.Bornemann, Y.Y.Li, J. Wuttke. Multiple Bragg reflection by a thick mosaic crystal. II. Solving the generalized Darwin-Hamilton equations on a lattice. *Acta Crystallographica Section A*. Draft to be submitted.
- [Fel] C. Felippa. Advanced finite element methods. Lecture notes, University of Colorado at Boulder.
- [Ham57] W.C Hamilton. The effect of crystal shape and setting on secondary extinction. *Acta Crystallographica*, 10:629–634, 1957.
- [J.P00] J.P.Boyd. *Chebyshev and Fourier Spectral Methods*. New York: Dover Publications, Inc., 2000.
- [Kop09] D.A. Kopriva. *Implementing Spectral Methods for Partial Differential Equations*. Springer Netherlands, 2009.
- [NM116] NM13. Characteristics of neutrons, 2016.
- [N.W76] N.W. Ashcroft, N.D.Mermin. *Solid State Physics*. Cengage Learning, 1976.
- [Rot03] T. Rothman. *Everything's Relative and Other Fables in Science and Technology*. John Wiley & Sons., 2003.
- [Sea89] V.F. Sears. *Neutron Optics*. Oxford Universtiy Press, Inc., 1989.
- [Sea97] V.F. Sears. Bragg Reflection in Mosaic Crystals. I. General Solution of the Darwin Equations. *Acta Crystallographica Section A*, 53:35–45, 1997.
- [Tre01] L.N. Trefethen. *Spectral Methods in Matlab*. Society for Industrial and Applied Mathematics, 2001.
- [W.H15] W.H. Bragg, W.L. Bragg. *X Rays and Crystal Structure*. London: G.Bell and Sons, Ltd., 1915.
- [Wut14] J. Wuttke. Multiple bragg reflection by a thick mosaic crystal. *Acta Crystallographica Section A*, 70:429–440, 2014.